Tuning the band-gap and enhancing the trichloroethylene photocatalytic degradation activities of flower-like Ni-doped SnS_2/SnO_2 heterostructures by partial oxidation

Nasim Afzali [a], Mostafa Torka Beydokhti [a], Abbas Ali Khodadadi [a,*], Yadollah Mortazavi [a]

[a] *Catalysis and Nanostructured Materials Research Laboratory, School of Chemical Engineering, College of Engineering, University of Tehran, P.O. Box 11155/4563, Tehran, Iran*

Editor: Dr. G. Palmisano

Keywords:
Flower-like
Tin disulfide
Oxidation
Doping
Photocatalysts

A B S T R A C T

A hydrothermal procedure was used to synthesis flower-like 0–0.5 wt% Ni-doped SnS_2, oxidation extent of which was tuned in air at 350 °C for various times. Photocatalysts were dip-coated on coiled wire-meshes including a light source for oxidation of 500 ppm trichloroethylene in air. FE-SEM revealed that the SnS_2 flower-like structure integrity was preserved after partial oxidation, while surface areas were dramatically enhanced. XRD, HR-TEM, Raman, XPS and PL showed formation of fine crystalline nanoparticles and defects by oxidation and resulted in enhanced photocatalytic activity. Band gaps and defects recombination rate of heterostructures were tuned by partial oxidation and Ni doping. 43% oxidation of 0.34 wt% Ni-doped SnS_2 results in increased surface area by 7.7 times to 100 m^2/g, quenched electrons and holes recombination, increased the band gap, and showed the highest TCE conversion of 88%, while the photocatalyst with no oxidation showed no activity. Further addition of Ni declined the surface area and photocatalytic conversion.

1. Introduction

It is vital to remove air VOCs which cause detrimental damages to humankind's health and ecology system [1–3]. Among the VOCs, trichloroethylene (TCE) is an organochloride compound used as a solvent in industries for degreasing and cleaning purposes [4]. In 2012, International Agency for Research on Cancer has classified TCE as Group 1 of carcinogenic substances to humans [5].

Recently, among the various TCE removal methods, photocatalytic oxidation due to its room-temperature operation, its complete elimination into nontoxic CO_2 and H_2O products, and being cost-effective has received tremendous attention in academic and industrial research [1,3,6].

Photocatalysts are designed, fabricated and modified to improve the fundamental photocatalytic steps including (i) light absorption; (ii) transfer and separation of electrons and holes; and (iii) surface catalytic reactions [7,8]. Different intensification strategies such as structure and morphology improvement (size, crystallinity and shape), composition and support, defect engineering (doping, vacancies and disorders) and semiconductor heterostructures have been performed to maneuver the three basic photocatalysis steps toward an efficient charge kinetics process and photocatalytic activity, especially for TCE degradation [8–11]. Even though the majority of recent studies have been performed on photocatalytic oxidation of TCE in liquid phase [12–20], various attempts have been evaluated toward more efficient semiconductor-based photocatalytic oxidation of TCE in air.

TiO_2 catalyst, due to its low cost and high durability, has been by far the most common catalyst for photocatalytic TCE degradation in air; however, TiO_2 suffers from a wide band gap and low charge transmission efficiency [21–27]. Regarding TiO_2 modification, effects of structure shape [28], crystal phase and particles size [29,30] have been studied on TCE degradation in air. Besides, TiO_2-sepiolite hybrid materials [31], silica-supported titania [32], zeolite–TiO_2 hybrid composites [33,34] and TiO_2/WO_3 nanocomposites [35] have been constructed for photocatalytic oxidation of TCE in air. Also, other than TiO_2, zeolite/WO_3–Pt hybrid photocatalysts were used for TCE degradation in air [36]. Specifically, researchers have put major efforts into promoting photocatalytic efficiency even under visible light through doping of TiO_2 based materials. Thoroughly, various dopants, Pd [37], Pt [37–40], Fe [40–42], Ni and Cr [40,42], Co [42], $Ca(OH)_2$ [40], Cu [40,43,44], Mo,

* Corresponding author.
E-mail addresses: nasimafzali12@gmail.com (N. Afzali), mostafa.torkabeydokhti@kuleuven.be (M. Torka Beydokhti), khodadad@ut.ac.ir (A.A. Khodadadi), mortazav@ut.ac.ir (Y. Mortazavi).

Nb and W [42] and N [45], have been employed for improving physicochemical properties of crystalline and amorphous phases of TiO_2. Heterostructure and doping have been considered as promising ways to enhance photocatalytic degradation activities [8–10,46]. Design and optimization of a heterojunction between two semiconductors can overcome the limits of individual components. In addition, the selection of appropriate heteroatom and optimization of dopant amount lead to the creation of point defects such as oxygen vacancies in bulk and surface of semiconductors. Optimizing the structure and interface of heterojunctions alongside the elemental doping can enhance the separation of electrons and holes, excitons mobility, light-harvesting ability, surface reactions and consequently photocatalytic efficiency.

SnS_2 is an n-type direct band-gap (2.19–2.41 eV) semiconductor that is innocuous and relatively inexpensive [47–50]. SnS_2 has been proved to be a promising photocatalyst under visible light and short-wavelength near-infrared irradiation due to its narrow band gap [50–52]. However, being prone to photocorrosion, sluggish photoinduced electrons and holes separation and valence band endowing holes with low oxidation ability restrict its photocatalytic efficiency [50,52–54]. On the other hand, SnO_2 as an n-type semiconductor has a direct wide band gap from 3.2 to 3.72 eV [47,48,54,55]. The light-harvesting ability of SnO_2 is limited to the UV region of solar light [48,56]. SnO_2 exhibits excellent electron mobility and prominent oxidation ability of valence holes; nonetheless, it still suffers from fast recombination of charge carriers [57,58]. There is a type-II heterostructure between SnS_2 and SnO_2 due to their matched band potentials because both conduction and valence band edges of tin sulfide are more negative than tin oxide [50,58]. The difference in the chemical potential of sulfide and oxide causes a band bending at the heterostructure interface, inducing an internal electric field [46]. Strong interaction and tight-contact heterointerfaces of coupled semiconductors serve as charges transfer channels, so the formed built-in electric field effectively facilitates a spatial transfer and separation of electron-hole pairs and diminishes recombination of charge carriers. Also, SnS_2 can act as a photosensitizer for SnO_2 and brings the photocatalytic activity about the entire solar light range [49,55,59]. It has been demonstrated that structure, morphology, crystal phase, and particles size depend on the preparation methods. By a rational design of structure and morphology of SnO_2-SnS_2 heterostructure, light absorption efficiency can be tuned and the interfacial charge transfer and surface catalytic reactions can be facilitated to satisfy three basic steps of photocatalysis.

Different strategies have been conducted to fabricate SnO_2-SnS_2 heterojunctions for practical applications such as photocatalysis [48–50,54,55,58–62]. Moreover, some methods like composing with other semiconductors [63,64], depositing on support [56] and heteroatom doping [65], as well as introduction of vacancies [52,63], have been employed to improve SnO_2-SnS_2 heterojunction abilities for pollutants photocatalytic degradation. Thermal oxidation is a convenient and repeatable strategy for introduction of zero-dimensional (0D) particles of SnO_2 into two-dimensional (2D) SnS_2 nanosheets [49,62,66]. 2D SnS_2 owns a short-length stacked layered structure along (001) direction in which the layers will be gradually oxidized via prolonged partial oxidation [62]. The thin layered 2D SnS_2 possesses a higher proportion of coordinatively unsaturated atoms [8,67], which can initiate oxidation nucleation and growth. By partial oxidation, SnO_2 tends to create spherical particles to reduce surface energy so that many ultrafine nanoparticles will be formed. Three-dimensional (3D) flower-like SnS_2 consists of many 2D nanoplates as building blocks. Such a 3D flower-like structure, because of its nano-sized 2D building blocks, possesses a hierarchical porous structure, more coordinatively unsaturated atoms like sulfur vacancies on surface, higher surface/volume ratio and higher light-harvesting [68,69]. 0D SnO_2 benefits from larger surface area, small crystals size and more lattice defects and enhanced charge carriers mobility [70,71]. Flower-like SnS_2 serves as a uniform and non-restructuring template for the formation of monodispersed 0D-3D SnO_2-SnS_2 heterostructures by partial oxidation. Design of such a hierarchical heterostructure by partial oxidation paves the way for tuning band structures, optimizing interface structure by controlling SnO_2 content, regulating number of defects like oxygen vacancies that are abundant in nano-sized metal oxides [9,63], and surface area for higher photocatalytic efficiency.

Further, doping can be used to modify the characteristics of SnO_2-SnS_2 heterostructures. Doping and oxygen and sulfur vacancies are classified as point defects and realized either as bulk or surface defects [8]. Defect engineering, especially doping, can be performed on separate components of heterostructures and their interface to enhance optoelectronic properties [8]. If the radii of the dopant ion are comparable with that of the host atom, the existing lattice ion will be replaced by dopant, while dopant with almost lower radii will occupy interstitial positions in lattice [8]. Ni has been chosen as the dopant for defect engineering of the hierarchical heterostructure: (i) Due to close ionic radius of Ni^{2+} and Sn^{4+}, Ni can be successfully doped into flower-like SnS_2 that takes advantage of layered structure for homogeneous dispersion of dopants [72,73]; (ii) Generally, metal cation dopant can create a mid-gap state within band structure of SnO_2 and SnS_2 either under the conduction band and above the valence band edges or both of them, so the electronic states reduce band gap and extend light absorption range [74,75]; (iii) The electronic states because of doping act as trap centers for photogenerated electrons and holes, which facilitate charge carriers separation. Also, dopants on surface trap excited electrons and holes and improve their separation to react with electron acceptors or donors in photocatalytic systems [66,75]; (iv) Ni doping creates more homogeneous distributed sulfur vacancies at the lattice of SnS_2, serving as reactive centers for oxidation [65,76]; (v) Incorporation of Ni^{2+} into the lattice of SnO_2 during oxidation inhibits crystal growth, leading to formation of smaller particles [66]; (vi) Dopants on surface of semiconductors act as reactive centers for photocatalytic reaction processes [8,75].

Herein, we have synthesized flower-like 0–0.5 wt% Ni-doped SnS_2 through a facile and inexpensive one-step hydrothermal method. Ni-doped SnS_2-SnO_2 ternary photocatalysts were prepared by thermal oxidation of Ni-doped SnS_2. The morphology, heterostructure and optical properties of the photocatalysts were regulated by changing SnO_2 and Ni contents. For the first time, the as-prepared photocatalysts were used for photocatalytic oxidation of TCE in dry and humid air under UV and visible light irradiation.

2. Experimental

2.1. Synthesis of flower-like Ni-doped SnS_2

Tin(IV) chloride liquid ($SnCl_4$, 99.995%), L-cysteine powder ($HSCH_2CH(NH_2)CO_2H$, $\geq$ 97%) and nickel(II) chloride hexahydrate ($NiCl_2.6\ H_2O$, 99.9%) were purchased from Merck. Regarding the hydrothermal process to prepare flower-like 0.34 wt% Ni-doped SnS_2, first, 4 ml of 1 M $SnCl_4$ aqueous solution and 1 g L-cysteine were dissolved in 120 ml deionized water and stirred at 400 rpm for 30 min to achieve a transparent solution. Secondly, 1.6 ml of 0.05 M aqueous solution of $NiCl_2.6\ H_2O$ was added into the mixture and then well mixed by ultrasonication for 15 min. Finally, the homogenous solution was put in a Teflon-lined stainless-steel autoclave and subsequently heated at 160 °C for 24 h in an electric oven. The brownish-black product was washed with distilled water to remove unconverted precursors and template. Washing was done several times to reach distilled water pH of 7–8. Eventually, the products were dried in a vacuum oven at 60 °C for 12 h. Pure SnS_2 and 0.5 wt% Ni-doped SnS_2 were synthesized similar to the above method, without and with Ni precursor (1.6 ml, 0.15 M aqueous solution of $NiCl_2.6\ H_2O$), respectively.

2.2. Ni-doped SnS_2 partial oxidation in air

To prepare Ni-doped SnO_2/SnS_2, the virgin Ni-doped SnS_2 was

partially oxidized by heating the samples at 350 °C under pure air (99.999%) flow for different periods of time. This temperature was selected from a temperature-programmed oxidation (TPO) profile of Ni-doped SnS_2. Fig. 1 shows the TPO test result for Ni-doped SnS_2 sample in air, indicating FTIR peak areas in the range from 1290 to 1410 cm^{-1} of effluent SO_2 depicted versus temperature from room to 900 °C temperature. 350 °C as a medium temperature for controlled oxidation of Ni-doped SnS_2 samples was selected.

For each oxidation run, 200 mg sifted powder of Ni-doped SnS_2 was packed in a quartz reactor placed in the vertical furnace and degassed under 50 ml/min Argon (99.999%) flow passed through an oxygen trap at 100 °C for two hours, and then cooled to ambient temperature. Afterward, Argon was switched to pure air, which its flowrate was adjusted at 20 ml/min and then the temperature was elevated to 350 °C by ramping the furnace temperature at 5 °C/min and kept at this temperature for different periods of time, followed by cooling to room temperature. The effluent gas was passed through the gas cell of an online Bruker (VECTOR 22) Fourier transform infrared spectroscopy (FTIR) instrument to track released SO_2 gas concentration by recording spectrums every 2 min with an accumulation of 20 scans at a resolution of 5 cm^{-1}. The amount of SO_2 at each recorded FTIR spectrum was determined by comparing its characteristic peak area with the area of SO_2 peak obtained from a calibrated gas mixture (5000 ppm in Argon).

The samples without Ni doping, not oxidized and oxidized for 20 and 300 min with 0%, 43% and 100% oxide contents are denoted as 0Ni0Ox, 0Ni43Ox and 0Ni100Ox, respectively. The samples that were doped with 0.34 wt% Ni, not oxidized and oxidized for 0, 10, 20, 30, 50, 80, 100 and 300 min at 350 °C with oxide contents of 0%, 33%, 37%, 43%, 52%, 66%, 83%, 91% and 100% are denoted as 0.34Ni0Ox, 0.34Ni33Ox, 0.34Ni37Ox, 0.34Ni43Ox, 0.34Ni52Ox, 0.34Ni66Ox, 0.34Ni83Ox, 0.34Ni91Ox and 0.34Ni100Ox, respectively. In addition, the sample with 0.5 wt% Ni dopant that was oxidized for 20 min with 43% oxide content is denoted as 0.5Ni43Ox. All samples' specifications are presented in Table 1.

2.3. Characterization methods

The Ni element content was determined using an inductively coupled plasma-optical emission spectrometer (ICP-OES; SPECTRO ARCOS). The specific surface areas were measured by the single-point BET method in liquid N_2, employing a CHEMBET-3000 instrument. Before measurement, the samples were degassed at 100 °C for 2 h in Argon flow. The

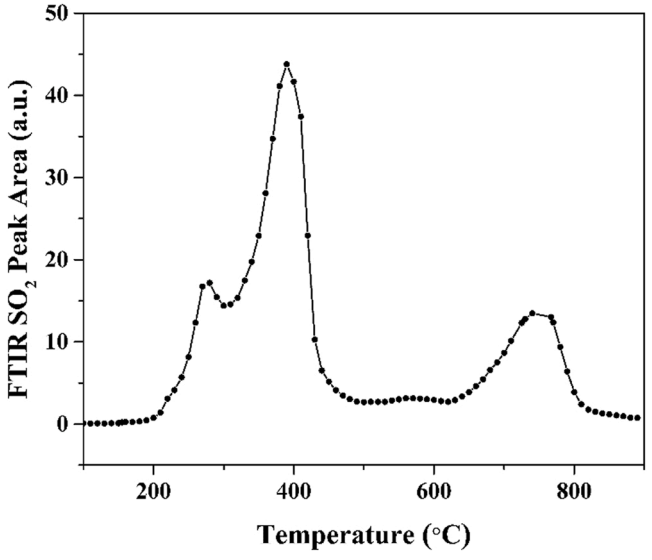

Fig. 1. Temperature-programmed oxidation (TPO) pattern of 20 mg Ni-doped SnS_2, 20 cc/min air, 5 °C/min.

Table 1
Photocatalyst samples name, Ni contents, oxidation time and percentages, crystallite sizes, adsorption, and conversion of 500 ppm of TCE in air with 250 ml/min flowrate on 0.5 g photocatalysts.

Sample name	Ni loading (ICP, wt%)	Oxidation duration at 350 °C (min)	Oxidation percent (SnO_2, mole %)	BET surface area (m^2/g)	Crystallite size (d_{XRD}, nm)	TCE adsorbed (μmole/g_{cat}) in dark condition	TCE adsorbed (μmole/m^2) in dark condition	TCE conversion at 40 min TOS (%)
No photocatalyst	–	–	–	–	–	0	–	0
0Ni0Ox	0	–	0	11	6.5	15	1.36	0
0Ni43Ox	0	20	43	85	–	46	0.52	78
0Ni100Ox	0	300	100	92	–	50	0.54	66
0.34Ni0Ox	0.34	–	0	13	4.5	20	1.53	0
0.34Ni33Ox	0.34	0	33	–	–	30	–	52
0.34Ni37Ox	0.34	10	37	–	–	41	–	63
0.34Ni43Ox	0.34	20	43	100	4	59	0.59	88
0.34Ni52Ox	0.34	30	52	–	–	45	–	44
0.34Ni66Ox	0.34	50	66	75	–	40	0.53	42
0.34Ni83Ox	0.34	80	83	–	–	48	–	67
0.34Ni91Ox	0.34	100	91	–	–	53	–	76
0.34Ni100Ox	0.34	300	100	101	4.5	56	0.55	77
0.5Ni43Ox	0.5	20	43	88	–	35	0.39	35

morphologies of the samples were observed using FE-SEM (MIRA3TESCAN-XMU) in conjunction with Energy-dispersive X-ray spectroscopy (EDX) and EDX mapping. The microstructure was analyzed by TEM and HR-TEM (FEI; Tecnai G^2 F20 S-TWIN field emission transmission microscope) operated at 200 kV as well as Fast Fourier transform (FFT) diffraction patterns. To prepare the sample before imaging, a suspension of the powder in 2-propanol was added dropwise on a copper-coated carbon TEM grid. The structure and crystallinity of materials were investigated by XRD from 5° to 100° on a Philips X'Pert Pro diffractometer with CuKα radiation (λ = 0.15406 nm). The average crystallite size of the samples was estimated from XRD patterns by Scherrer's equation [41]. The Raman spectra were obtained from a Raman spectrometer (Takram N1–541) supplied with a CCD detector using a 532 nm laser line in the wavelength range of 100–4600 cm^{-1}. PL spectra of samples were carried out using a fluorescence spectrometer (Varian Cary Eclipse) in a 200–800 nm wavelength with an excitation wavelength of 300 nm. The samples' optical absorption and band gap were performed by UV-Vis diffuse reflectance spectroscopy (Analytic Jena; SPECORD 250) in a spectral range of 190–1100 nm. The surface composition and phase of a sample were characterized using XPS (Gammadata-scienta ESCA200) with a monochromatic Al K_α (1486.6 eV) radiation source and C 1s (284.6 eV) reference.

2.4. Deposition of photocatalysts on galvanized steel wire mesh as substrates

Photocatalysts coating on wire mesh substrates, prior to activity tests, were in a similar fashion as presented in our group's previous work on the photocatalytic degradation of TCE on Fe-doped TiO_2 [41]. The photocatalysts were coated on galvanized steel wire mesh (Tyler series number 18) as substrates. A piece of wire mesh of 22 × 34 cm size was twisted into a hollow cylinder with five layers. The rolled cylinder was 22 cm in height with an external diameter of 2.5 and an internal diameter of 1.5 cm to place the lamp. Before coating, the substrates were washed with acetone and distilled water. The dip-coating method was used to deposit 0.5 g loading of photocatalysts so that the wire mesh substrates were dipped for 10 min into a 10 wt% aqueous suspension of grinded powders with an average size of 200 nm (measured by dynamic light scattering, DLS, Micromeritics, NanoPlus-1, Fig. S1) several times. The suspensions were dispersed by ultrasonication for 15 min. The coated substrates were dried at 100 °C for 30 min. An aluminum foil was used to cover the external surface of coated wire mesh substrate to reflect the lamp radiation into the reactor. A UV radiometer (VLX-3 W, Cole-Parmer) was used to measure UV light intensity inside the reactor. The intensity at the substrate's inner surface and outer surface (under the reflector foil) were 27 and 8 W/m^2, respectively (A and B positions, Fig. S2).

2.5. Photocatalytic degradation of TCE

The photocatalytic activity of as-prepared samples coated on the wire-mesh substrates was investigated for degradation of TCE in air through the same reaction system utilized in our group's previous work (Fig. S2) [41]. The effective volume of the annular reactor (25 mm OD, 16 mm ID and 25 cm height) was 67 cm^3 (Fig. S3). The feed of photocatalytic reaction was 500 ppm TCE in the air (99.999%) with a flow rate of 250 ml/min derived from mixing gaseous flows of 1000 ppm TCE in air and pure air. Photocatalytic reactions were done at 25 °C and atmospheric pressure. The feed and effluent gases from the reactor were analyzed at various times on stream (TOS) up to 40 min by an online gas cell in an FTIR spectrometer with an accumulation of 10 scans and resolution of 5 cm^{-1}. The conversion of TCE is calculated by Eq. (1):

$$\text{Conversion}(\%) = \frac{C_0 - C}{C_0} \times 100, \quad (1)$$

Where C_0 is the concentration of TCE in feed and C is the concentration of TCE in the effluent gas. The conversion of TCE was given after 40 min TOS unless it is stated otherwise. Bare wire mesh substrate was used for the degradation of TCE as the blank test. The effect of water vapor on photooxidation performance was probed by passing the air flow through a bubbler encompassing deionized water at room temperature to acquire about 50% relative humidity (RH) in the feed. A germicidal white light lamp (8 W, Philips, Holland) whose wavelength range is 200–300 nm with maximum intensity at 254 nm was used as the UV radiation source. Photooxidation activity under visible light was examined using a fluorescent visible light lamp (8 W, Philips, Holland) with a wavelength range of 380–740 nm.

3. Results and discussion

3.1. Partial oxidation of Ni-doped SnS_2

Fig. 2 exhibits the released SO_2 versus time for 20 mg Ni-doped SnS_2, derived from the TPO test (Fig. 1). Integration of the area under the curve provides the total amount of SO_2 for 20 mg of Ni-doped SnS_2.

The amounts of SO_2 released from 0.2 g of Ni-doped SnS_2 during partial oxidation in each run were estimated to calculate SnO_2 contents (Fig. S4). The amount of released SO_2 in each oxidation run divided by the total amount of SO_2 for 0.2 g of Ni-doped SnS_2 (10 times total SO_2 release from 20 mg Ni-doped SnS_2 oxidation in its TPO) provide oxidation percentage. Specifications of all as-prepared samples are listed in Table 1.

3.2. Characterization of photocatalysts

Fig. 3 shows the XRD patterns of some samples. No peak for impurity phases was detected in the patterns. The XRD pattern of pure SnS_2 is provided in the Fig. S5. No diffraction peaks related to the Ni dopant were observed, possibly due to its small amount or successful doping of Ni elements into SnS_2 and SnO_2 crystalline lattice structures [41,77].

The observed diffraction peaks at 15°, 28.34°, 32.17°, 41.9°, 50.14° and 52.42° for 0.34Ni0Ox sample are attributed to (001), (100), (101), (102), (110) and (111) crystal plates of SnS_2 hexagonal phase (JPCDS No. 23–0677), respectively. Nonetheless, unlike the SnS_2 reference pattern, the intensification of (101) and (110) planes peaks indicate the dominance of (101) and (110) preferred orientation of hexagonal SnS_2. Interestingly, the broadened and less strengthened (001) peaks at 15.2° for 0Ni0Ox and 15° for 0.34Ni0Ox imply that growth of SnS_2 layers was

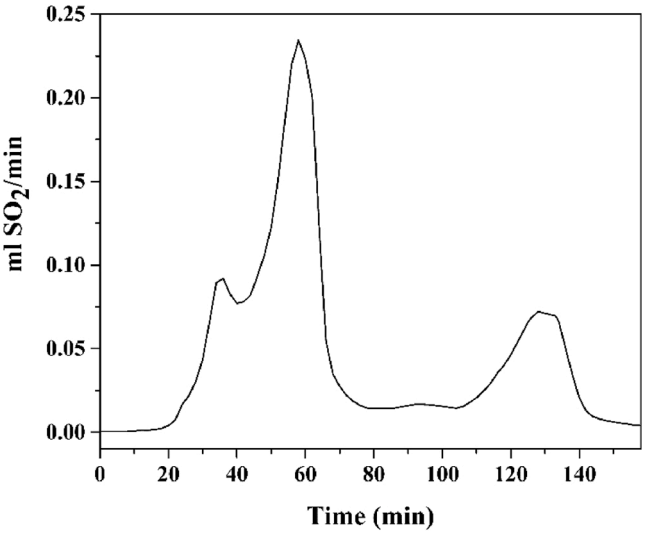

Fig. 2. Released SO_2 during TPO of 20 mg Ni-doped SnS_2 in air at 5 °C/min temperature ramp rate.

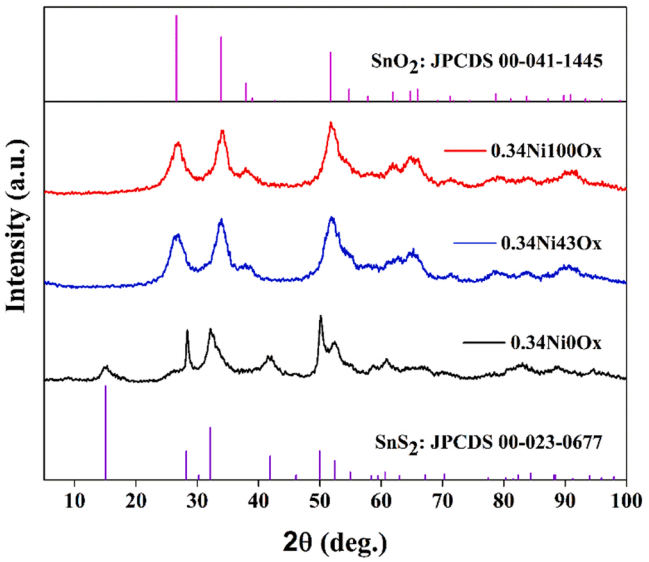

Fig. 3. XRD pattern of samples.

inhibited along the c-axis, indicating lattice expansion, causing d-spacing increase [76]. The (001) peak is transferred to lower degrees after doping (15.2 ° vs. 15 °), which means the d-spacing between Ni-doped SnS_2 layers become a bit larger than SnS_2 layers. Inter-layer enlargement and few-layered SnS_2 can be due to structural strain created by lattice expansion as a consequence of creation of more sulfur vacancies after Ni doping in crystal lattice [75]. Crystal matrix distortion because of Ni doping induces creation of smaller particles and disordered long-range structure [76,77]. The crystalline particles size of 0Ni0Ox and 0.34Ni0Ox corresponding to diffraction peaks at 32.17° are 6.5 nm and 4.5 nm, respectively (Table 1). The diffraction peaks at 2θ= 26.83°, 34.12°, 38°, 52°, 61.84° and 65.15° for 0.34Ni100Ox are corresponding to (110), (101), (210), (211), (220), (310) and (301) planes of tetragonal rutile phase of SnO_2 (JCPDS No. 41–1445). Incorporation of Ni into the lattice structure of SnO_2 nanoparticles formed during thermal oxidation, replacing Sn^{4+} (0.71 Å) by Ni^{2+} with a lower ionic radius (0.69 Å), leads to inhibiting crystal growth and forming smaller grain sizes [74,75]. This phenomenon has a good agreement with broadened diffraction peaks of SnO_2, indicating the creation of ultra-small particles. No remarkable differences were observed between 0.34Ni43Ox and 0.34Ni100Ox diffraction spectrums. However, the particles' crystallite size for 0.34Ni43Ox and 0.34Ni100Ox were 4.0 and 4.5 nm, respectively. This observation figures out SnO_2 particles have a small crystalline size so that the peaks intensification for 0.34Ni43Ox does not change compared to 0.34Ni100Ox via prolonged oxidation time and, consequently, increasing of SnO_2. Any diffraction peak was not detected related to hexagonal SnS_2 in 0.34Ni43Ox spectra, perhaps due to short-range order crystallinity because of oxidation of disordered long-range phases, tiny crystals and/or amorphous structure [76].

The morphology, structure and EDX characterizations of 0.34Ni0Ox and 0.34Ni43Ox samples were investigated with FE-SEM. Fig. 4A reveals that 0.34Ni0Ox was formed in a uniform hierarchical 3D flower-like structure with microsphere aggregates sizes in the range of 1–2 micrometers. It is figured out from the high-resolution image (Fig. 4B) that the clusters have a peony-like nanoflowers features, owning fewer petals density with more open structures. The petals consisted of hexagonal-like SnS_2 nanosheets with smooth surfaces, twisted and curled, vertically interconnected, extended outward routed from the center. Aggregation growth toward frizzy intertwining nanoflakes and self-assembling of these building blocks to create such a hierarchical structure stem from the intrinsic anisotropic nature of hexagonal SnS_2 tending to reduce surface energy [77-79]. The thickness of formed layers is about 10 nm making the structures more favorable for reactants diffusion during photocatalytic processes [78,80].

Based on previous studies, the final structure of prepared SnS_2 via hydrothermal method strongly depends on sulfur source and concentration as well as solvent and reaction temperature. However, the exact mechanism for the formation of flower-like SnS_2 is still unclear, the formation of such a 3D hierarchical structure within hydrothermal synthesis could be divided into subsequent stages [77,78,81,82–84] (i) hydrolysis, (ii) nucleation, (iii) aggregation of nuclei leads to hexagonal nanoplates, (iv) random angle-to-angle and edge-to-edge self--assembling of nanoflakes of SnS_2, (v) oriented growth of 3D flower-like structure by ripening process. Thermal oxidation did not change the 3D flower-like structure, as is shown in Fig. 4D. The magnified image (Fig. 4E) shows that ultra-small SnO_2 nanospheres were formed on Ni-doped SnS_2 nanoplates, the sizes of which were up to a maximum of 10 nm. This result is consistent with XRD data, assuming very small crystals size for SnO_2 particles. Creation of sulfur vacancies due to Ni dopant provides more reactive sites prone to oxidation that can initiate the growth of SnO_2 nanospheres by thermal oxidation. Incorporation of adjacent Ni alongside the growth of SnO_2 could reduce crystallinity and particles size. Preserving the flower-like structure, even after oxidation, clarifies the formation of a firm heterostructure between SnO_2 and SnS_2. The 0.34Ni43Ox benefits from not only enhanced charge transfer resulting from the formation of highly dispersed Ni-doped SnO_2 nanoparticles but also improved light-harvesting as a result of internal light reflection in flower-like structure [85]. Fig. 4C and F present EDX spectrums of 0.34Ni0x and 0.34Ni43Ox samples, respectively. 0.34Ni0Ox consists of Sn, S and Ni elements (Fig. 4C), which S was replaced by O after 20 min thermal oxidation, denoting 0.34Ni43Ox. The S, O and Ni elements distributions in the 0.34Ni0x and 0.34Ni43Ox samples are shown in Fig. 4G and H. It is noteworthy that the Ni was well distributed in the sample structure and the amount of the O element increased through thermal oxidation.

BET surface areas of samples are presented in Table 1. SnS_2 possesses a low surface area, but partial oxidation and doping dramatically increased the surface area. Formation of ultra-small SnO_2 particles by partial oxidation alongside preserving the hierarchical 3D flower-like structure significantly increases surface area. During partial oxidation, SnS_2 layers were oxidized gradually, while the layered structures remained unchanged [62]. Oxidation increases the density of SnS_2 by a factor of 1.5 that causes improvement of specific surface area. Also, SnO_2 forms a different morphology, i.e., hexagonal 2D nanoplates of SnS_2 are converted to tetragonal 0D nanoparticles, which reduces surface energy and increases surface area. The surface area can be tuned by partial oxidation to boost photocatalytic activity. By increasing SnO_2 contents from 43% to 66% and 100%, the BET surface area first declined from 100 m^2/g for 0.34Ni43Ox to 75 m^2/g for 0.34Ni66Ox and then increased again up to 101 m^2/g for 0.34Ni100Ox. By 66% oxidation, the surface area was reduced, possibly due to the formation of larger SnO_2 particles. The BET surface areas of heterostructures were dependent on doping as well as partial oxidation. Doping can increase surface area, as has been observed in other semiconductors, which may be due to the formation of smaller particles by doping [41]. 0.34 wt% Ni could increase the surface area of both SnS_2 and SnO_2. 0.34Ni0Ox has a surface area of 13 $m^2/$, higher than 11 m^2/g for 0Ni0Ox. Furthermore, the BET surface area of 0.34Ni100Ox is 101 m^2/g, while 92 m^2/g for 0Ni100Ox. Interestingly, 0.34Ni43Ox sample with 0.34 wt% Ni showed a surface area of 100 m^2/g, 15 m^2/g higher than that for 0Ni43Ox. By increasing dopant content from 0.34 to 0.5 wt% at 43% oxidation, the BET surface area was decreased to 88 m^2/g. The higher surface area provides more adsorption capacity and more active sites for photocatalytic oxidation.

The microstructure of 0.34Ni43Ox was further investigated by TEM and HR-TEM. According to Fig. 5A, 0.34Ni43Ox shows a uniform 3D flower-like structure consistent with FE-SEM results. The TEM image (Fig. 5A) reveals that the light areas were attributed to the thin planes laying along the substrate, while the dark ones indicate sheets perpendicular to the substrate. Also, it is visible that the intertwining and

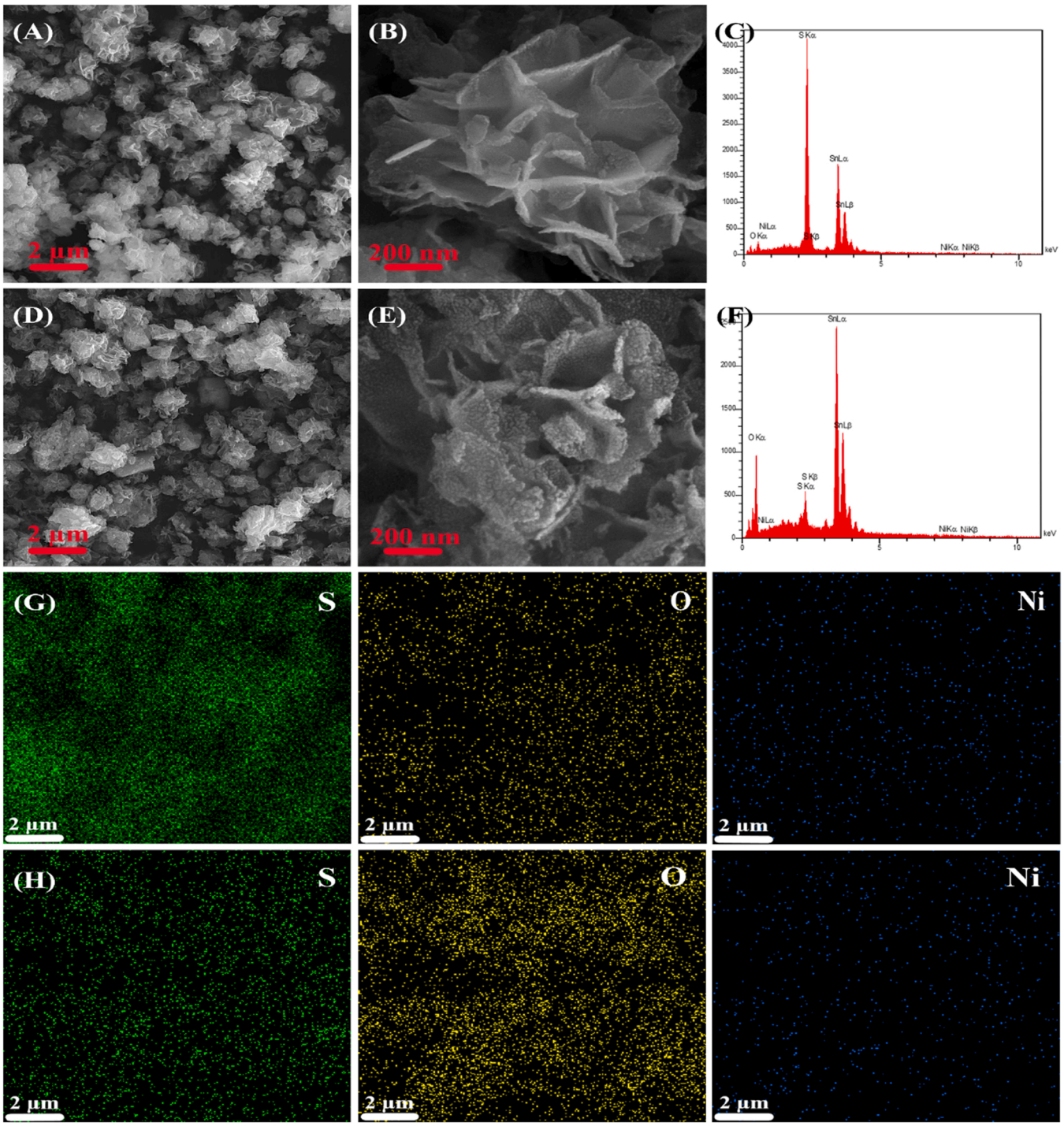

Fig. 4. FE-SEM images of 0.34Ni0Ox (A) and 0.34Ni43Ox (D) and their magnified images (B and E), EDS spectrums of 0.34Ni0Ox (C) and 0.34Ni43Ox (F) and elemental mapping of 0.34Ni0Ox (G) and 0.34Ni43Ox (H).

intertangling petals, consisting of nanosheets as building blocks, are closely packed across the core that can preserve structural integrity. Fig. 5B shows the polycrystalline nature of 0.34Ni43Ox consisting of lots of small particles of SnO_2 and SnS_2 in the range of 2–5 nm. As can be seen from Fig. 5B, the 0.316 and 0.278 fringe intervals are coincided with interplanar spacing of (110) and (101) crystal planes of SnS_2 hexagonal phase, whereas that of 0.334 and 0.264 correspond to the interplanar spacing of (110) and (101) crystal planes of tetragonal phase of SnO_2. None of the d-spacing was related to sulfide and oxide states of Ni, mainly because Ni content is very small and is well doped into the lattices of SnS_2 and SnO_2. Interestingly, the lattice of 0.34Ni43Ox is wholly deformed and not coherent, owning many defects and distorted areas. The boundary defects, observed between the lattice structures, corroborate tiny nanoparticles of SnS_2 and SnO_2. When the particles size is reduced, the bulk and surface defects are increased (Fig. S6). FFT diffraction patterns of A, B and C selected regions (yellow rectangles in Fig. 5B), presented in Fig. 5C, D and E, confirm the presence of SnS_2 hexagonal, SnO_2 tetragonal phases and formation of SnO_2/SnS_2 heterostructure, respectively. As a corollary, the morphological observations clarify the introduction of Ni-doped SnO_2 nanoparticles on Ni-doped SnS_2 nanosheets, leading to the construction of a tight heterostructure, providing a spatially favorable interfacial charge transfer.

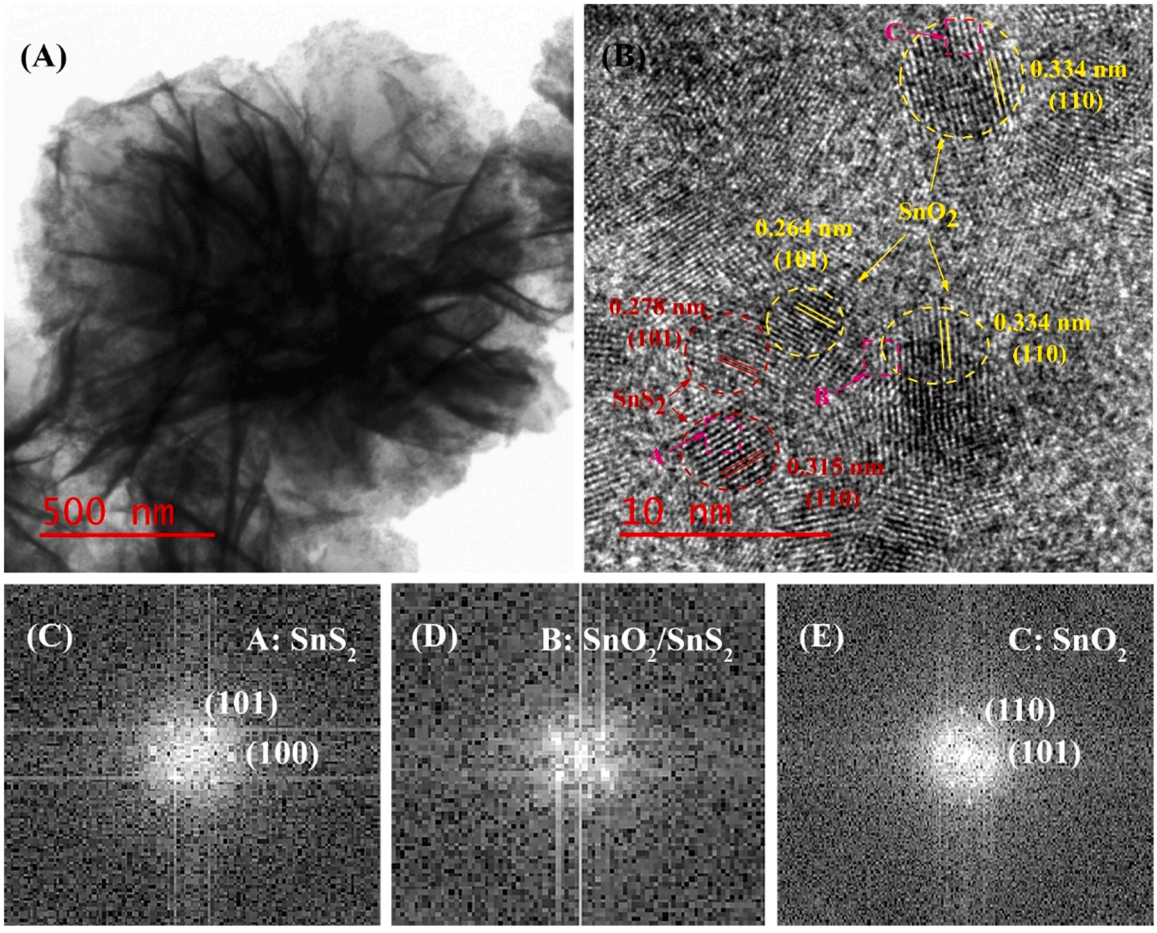

Fig. 5. TEM (A) and HR-TEM (B) images of 0.34Ni43Ox, FFT diffraction patterns of selected areas at B (C, D and E).

Unlike the XRD, the Raman is not only dependent on long-range orders. The Raman spectra of samples are shown in Fig. 6. CdI_2-like hexagonal SnS_2 possesses a singly degenerating active mode of A_{1g} that Sn atom is static and two S atoms have an out-of-phase displacement with respect to each other parallel to the c-axis [86]. For 0.34Ni0Ox, the peak at 308 cm^{-1} is assigned to the characteristic Raman peak of A_{1g} mode [55,58,59,64].

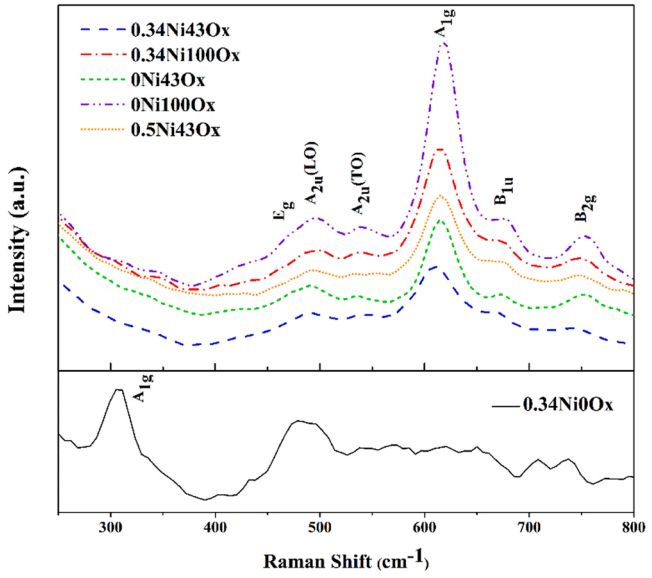

Fig. 6. Raman spectra of the photocatalyst samples.

Tetragonal rutile SnO_2 has 15 lattice vibrational modes in the center of the Brillouin zone, which is given by Eq. (2) [87]:

$$\Gamma = 1A_{1g} + 1B_{1g} + 1B_{2g} + 1E_g + 1A_{2g} + 1A_{2u} + 2B_{1u} + 3E_u \quad (2)$$

Where the A_{1g}, B_{1g} and B_{2g} non-degenerate modes plus doubly degenerate E_g mode are Raman active due to interior phonon and known as volume modes [88]. The A_{1g}, B_{1g} and B_{2g} modes are related to the vibration of Sn-O in the plane perpendicular to the c-axis, while the E_g mode is due to the vibration of oxygen in the direction of the c-axis [87, 89]. The A_{2u} and E_u (Sn and O vibrating with plane perpendicular to c-axis), which are TO (transverse-optical vibration) and LO (longitudinal-optical vibration) modes, are IR active and the A_{2g} and B_{1u} (vibration of Sn and O in the direction of c-axis) symmetries are silent modes [89–91]. These modes are classified as surface phonon modes [88,92]. The E_g mode is the most sensitive mode to the oxygen vacancies [87]. Presence of E_g mode in 0.34Ni0Ox sample indicates the creation of oxygen vacancies on the surface because of room-temperature oxidation of highly active sulfur vacancies. After thermal oxidation, even for 20 min, the characteristic peak of SnS_2 was disappeared. The raised shoulder at 482 cm^{-1} and peaks at 614 and 746 cm^{-1} for oxide samples Raman spectra correspond to E_g, A_{1g} and B_{2g} vibration modes, respectively [58,59,91]. The intensity and broadness of A_{1g} can be due to size effect, crystallinity and oxygen stoichiometry. Increasing particles' size and degree of crystallinity and supplying the oxygen vacancies in sub-stoichiometric samples with oxygen by prolonged partial oxidation can intensify the A_{1g} mode peak [87,93]. The 0.34Ni43Ox has the broadest and less intensified A_{1g} peak, possibly due to smaller particles' size and more surface defects. By oxidation to 100%, for 0.34Ni100Ox,

the A_{1g} mode peak becomes sharper, indicating growth of larger SnO_2 particles and lower vacancies. The A_{1g} peak intensity increases for 0Ni43Ox and 0Ni100Ox compared to 0.34Ni43Ox and 0.34Ni100Ox, respectively. It is concluded that doping induced size and crystallinity reduction and could produce more oxygen vacancies. Increasing Ni dopant content to 0.5 wt%, 0.5Ni43Ox, causes intensification of A_{1g} peak and then larger particles size. There also exist two peaks at 497, 538 cm^{-1} and a shoulder at 673 cm^{-1} that are assigned to A_{2u} (TO), A_{2u} (LO) and the forbidden Raman B_{1u} modes [59,89,92,94]. Activation of these surface phonon modes is due to the vibration of surface atoms because of increasing surface-to-volume ratio as a consequence of reduction of particles size and/or increase of disorder and surface defects as a result of converting from crystalline to amorphous phase [88, 89,92,94,95]. Partial oxidation and Ni doping are promising ways to tune the particles' size and, subsequently, surface defects such as oxygen vacancies to promote photocatalytic activity.

Fig. 7 represents results of the XPS analysis of 0.34Ni43Ox. The survey spectrum, Fig. 7A, sheds light on the existence of Sn, S and O elements in the 0.34Ni43Ox sample. The presence of the C element in the spectrum is due to the hybridization of foreign carbon-based contaminants. The C 1s standardized binding energy, 284.6 eV, was used to calibrate binding energies in the XPS spectra. In the magnified spectrum of Sn 3d (Fig. 7B), there are two peaks located at 487.23 and 495.63 eV, which are attributed to Sn 3d5/2 and Sn 3d3/2, respectively [55,62]. The spin-orbit splitting between two peaks is 8.4 eV, suggesting the presence of valence state of Sn^{4+} in the heterostructure [59,96]. The deconvolution of high-resolution spectra of S 2p (Fig. 7C) discloses that two peaks at 161.1 and 162.15 eV, with a splitting energy of 1.05 eV own to spin-orbit coupling, are related to S 2p3/2 and S 2p1/2 doublets of S^{2-} in the 0.34Ni43Ox [59,97]. The O 1s core-level spectroscopy in Fig. 7D can be deconvoluted to three photoelectron peaks at the binding energy of 530.7, 531.7 and 533.2 eV. The peak at 530.7 eV is assigned to the binding energy of O^{2-} in SnO_2 lattice structure. In other words, this peak shows the number of oxygen atoms in a fully oxidized stoichiometric region. The peak centered at 531.7 eV originates from oxygen in oxygen-deficient regions of surface SnO_2. Actually, this peak can be attributed to surface-adsorbed oxygen, which can only chemically adsorb on oxygen vacancies at the surface. The intensity of peak at 531.7 eV is higher than peak at 530.7 eV because quantity of oxygen vacancies is more than that of oxygen atoms in fully oxidized stoichiometric regions at surface layers of 0.34Ni43Ox heterostructure. Additionally, the peak at 533.2 eV associates with surface hydroxyl group [63,98,99].

UV-Vis diffuse reflectance spectra of the photocatalyst samples are presented in Fig. 8. The 0Ni0Ox and 0.34Ni0Ox show boosted not only visible light absorption but also UV light absorption ability. It is found that such a flower-like structure exhibits a significant light-harvesting ability, which is beneficial for producing more photoinduced charge carriers. Nonetheless, the 0Ni100Ox and 0.34Ni100Ox only exhibit a significant light absorption in the UV region. Forming a heterostructure between SnS_2 and SnO_2 by partial oxidation of SnS_2 is a strategy to tune the light absorption ability for efficient photocatalytic activities. By increasing SnO_2 content to 43% and 66%, the absorption edge shifts to lower wavenumbers toward the light absorption range of pure SnO_2. It is

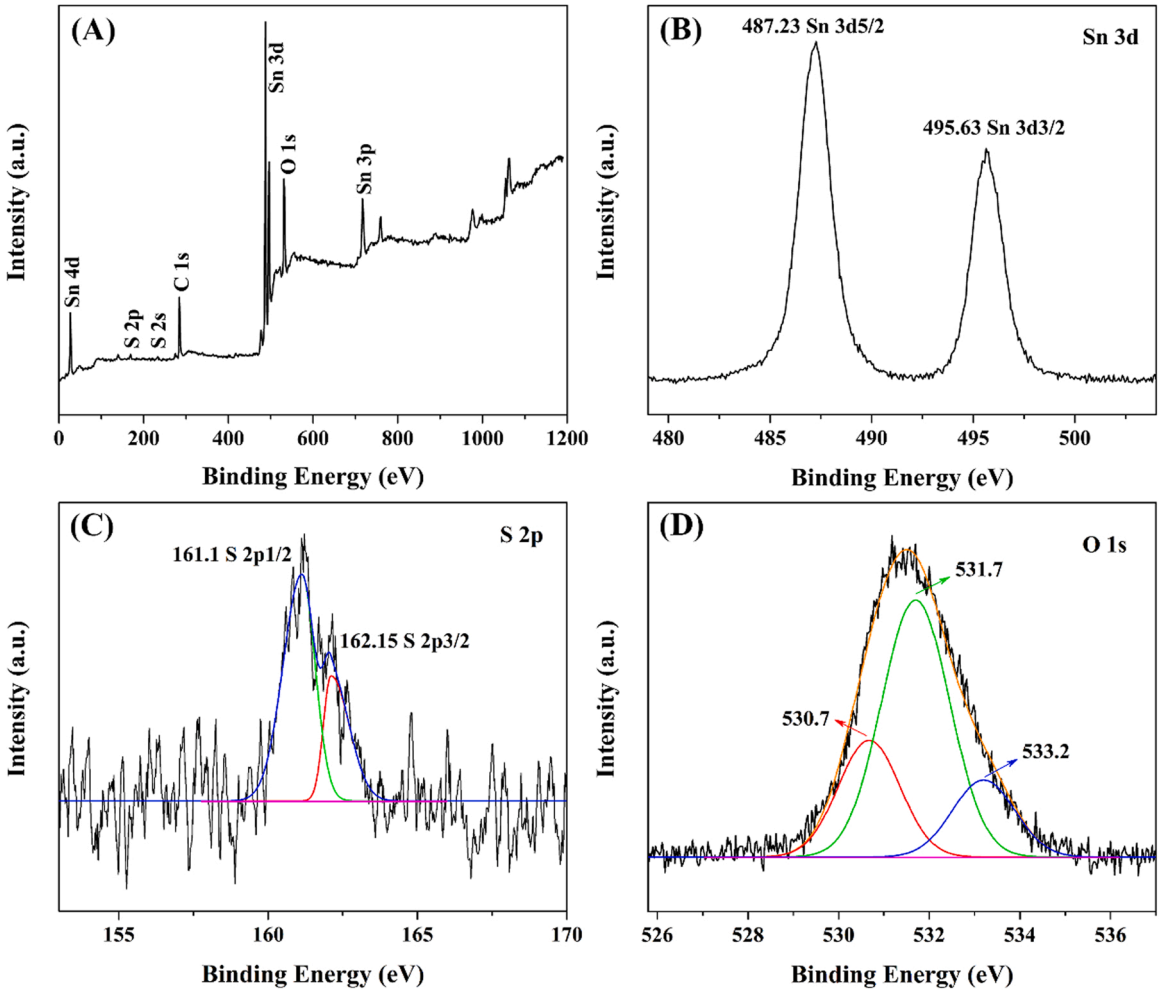

Fig. 7. XPS spectrum of 0.34Ni43Ox: Survey (A), Sn 3d (B), S 2p (C) and O 1s (D).

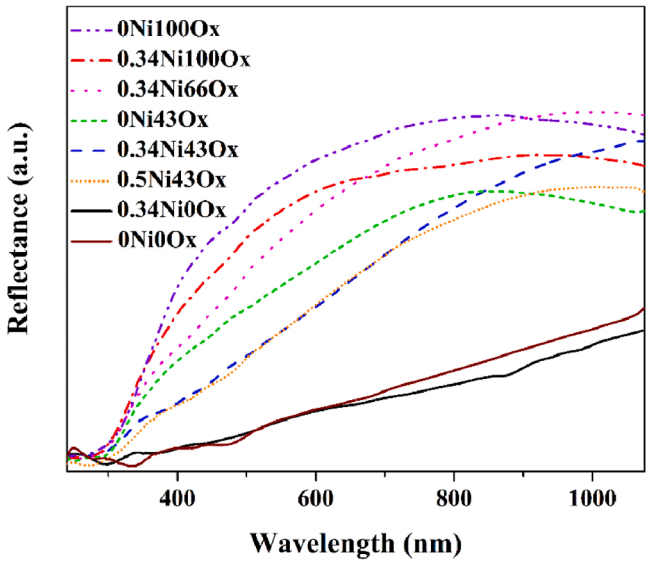

Fig. 8. UV–vis diffuse reflectance spectra of the samples.

noteworthy that the absorption edge of 0.34Ni0Ox, 0.34Ni100Ox and 0.34Ni43Ox had a redshift compared to 0Ni0Ox, 0Ni100Ox and 0Ni43Ox. Incorporating Ni^{2+} into lattice structure causes the s, p-d hybridization and local disorder because of a lower ionic radius than Sn^{4+}, leading to a change in local electronic structure [100]. Increasing Ni dopant from 0.34 to 0.5 wt%, 0.34Ni43Ox versus 0.5Ni43Ox, does not make a significant change in light absorption ability.

The direct band gaps were calculated based on the Kubelka-Munk equation [50,62], shown in Fig. 9A and B.

The band gaps of 0.34Ni0Ox, 0.34Ni100Ox and 0.34Ni43Ox are 1.81, 3.39 and 2.64 eV, while those of 0Ni0Ox, 0Ni100Ox and 0Ni43Ox are 1.87, 3.45 and 3.1 eV. Partial oxidation of SnS_2 causes taking advantage of photocatalysis properties of SnO_2 nanoparticles beside narrowing band gap of SnO_2 to photocatalytic activity in the entire range of the solar light. Increasing oxidation from 0% to 100% causes an increase in the band gap. Obviously, dopant induces band gap renormalization, regarding Ni impurity level in the band structures of pure SnS_2 and SnO_2, creates an energy level close to the lower state of the conduction band and shrinks the band gap [101]. Exchanging of Ni^{2+} with Sn^{4+} induces a charge imbalance in SnS_2 and SnO_2 lattice, which creates structural defects such as S and O vacancies that can act as an electron donor near the conduction bands of SnS_2 and SnO_2. The band gap shrinkage is due to mutual exchange and the Coulomb interactions between the added free electrons in the conduction band and electron-impurity scattering [102]. Interestingly, the effect of Ni doping on band gap narrowing is higher when there is a SnO_2/SnS_2 heterostructure. The formation of SnO_2 particles smaller than 5 nm on SnS_2 nanosheets will increase defects such as boundary ones, which is also realized from the HR-TEM image. Ni can be better doped in the interface, defects and boundaries when there is a heterostructure between SnO_2 and SnS_2, thus the effect of Ni doping on the band gap can be higher than the individual components [8]. The band gap of 0.5Ni43Ox is slightly lower than 0.34Ni43Ox. As a result, oxidation of 0.34Ni0Ox up to 43% leads to a heterostructure that possesses an extended light-absorbing ability from UV to visible light ranges, indicating a promising photocatalyst not only under UV light but also under visible light irradiation.

Fig. 10 A depicts PL intensities of prepared samples. The PL emission can be related to recombination of electrons and holes at bulk, interface and surface of heterostructures. The PL peaks can be attributed to both the radiative and non-radiative relaxation processes [103]. Radiatively occurs by photon energy emitted from direct recombination of conduction band electrons and valence band holes. Non-radiatively occurs by emitting phonon from recombination of carriers through defect states such as dopant and vacancies in bulk and surface and interface channels in heterostructures particles [103–105]. Maximum intensities of PL emission of samples are presented in Fig. 10B (at 360 nm). Creating a heterostructure between SnO_2 and SnS_2 enhanced charge carriers' separation and transition and suppressed electron-hole recombination as observed in other SnO_2 and SnS_2 heterostructures [58,62]. Recombination of electrons and holes in SnO_2/SnS_2 heterostructures are lower than 0.34Ni0Ox and 0.34Ni100Ox, but the recombination rate is minimum at specific SnO_2 content. 0.34Ni43Ox and 0Ni43Ox show the lowest PL intensities, suggesting a lower recombination probability. Interfacial transfer and separation of photogenerated electrons and holes at the internal electric field are tuned by partial oxidation of flower-like Ni-doped SnS_2. The PL intensities of 0.34Ni43Ox and 0.34Ni100Ox are lower than 0Ni43Ox and 0Ni100Ox, respectively. Clearly, Ni doping quenches the PL intensity because Ni acts as electron trapping centers, which enhance electron-hole separation, in other words, enhance the non-radiative recombination process [66,106]. Increasing Ni dopant to 0.5 wt%, 0.5Ni43Ox, enhances PL intensity. A shorter distance of Ni-Ni ions at higher contents of Ni that leads to transfer energy between nearby ions can increase PL intensity, consequently reducing electron-hole separation efficiency [41]. Optimizing a heterointerface between SnS_2 and SnO_2 and defects engineering such as tuning doping and oxygen vacancies can be an efficient path to improve

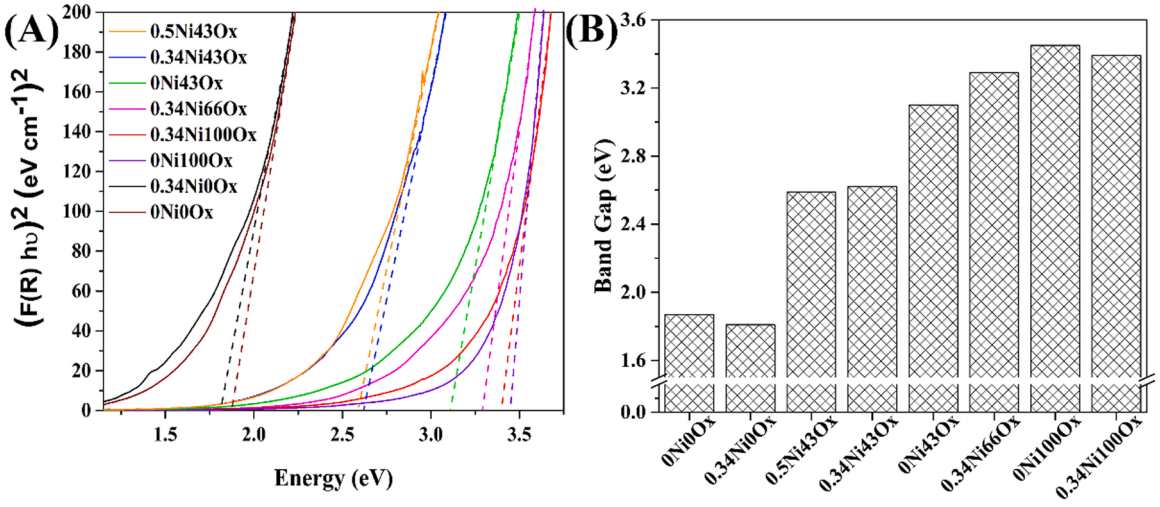

Fig. 9. $(F(R)\ h\upsilon)^2$ vs $h\upsilon$ plots (A) and optical band gaps of the samples.

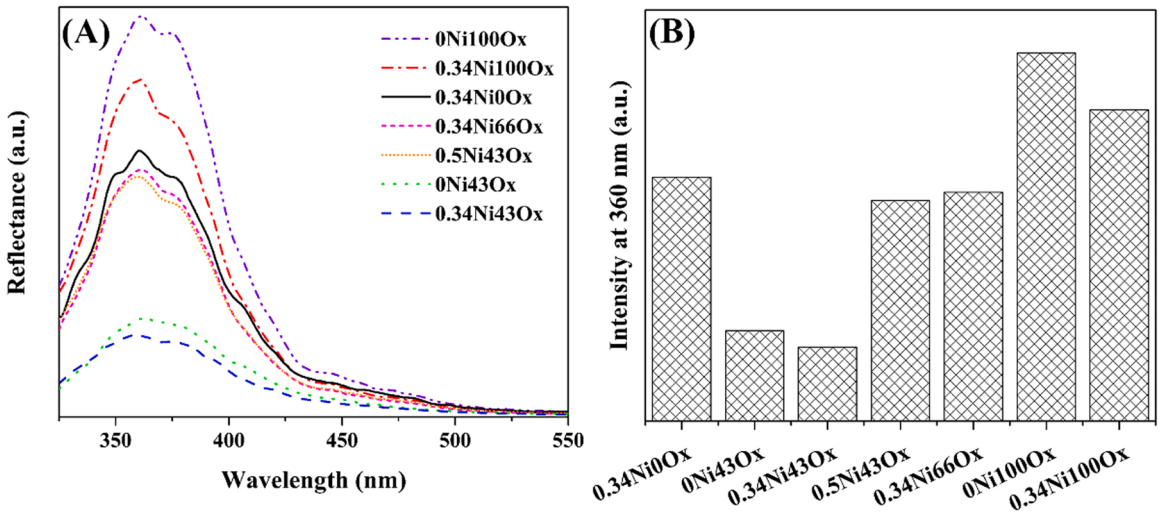

Fig. 10. (A): Photoluminescence spectra of photocatalyst samples and (B): maximum intensity at 360 nm.

electron-hole separation and transmittance.

3.3. Photocatalytic activities

3.3.1. Photocatalytic oxidation products

Fig. 11 A shows FTIR spectra of feed, 500 ppm TCE in the air, and Fig. 11B exhibits the effluent gas of photocatalytic reactor for 0.34Ni43Ox after 40 min TOS.

The FTIR peaks located at 631 and 873 cm^{-1} are assigned to C-Cl and at 838 and 3096 cm^{-1} to C-H bending vibration, which correspond to TCE. The bands around 1631 and 3780 cm^{-1} are attributed to the H-O-H bending of water molecules. For Fig. 11B, the peaks at 2143, 2331 and 2349 cm^{-1} are related to CO and duplet O═C═O bending vibrations [41]. No characteristic peaks are observed for dichloroacetyl chloride (DCAC, $CHCl_2COCl$), phosgene (Cl_2CO) and trichloromethane ($CHCl_3$) as other products of photocatalytic oxidation of TCE [107]. So, CO_2, H_2O and a minor amount of CO and HCl were only products of degradation of TCE on 0.34Ni43Ox.

3.3.2. Adsorption and degradation of TCE on photocatalysts

Fig. 12 shows the adsorption of TCE on the photocatalyst samples in the dark condition and its degradation on the photocatalysts under UV light. Adsorption capacities of the samples in dark condition (explained in Supplementary material) and their photocatalytic conversion after 40 min TOS are presented in Table 1. Adsorption and activation of TCE on the photocatalysts surface is an essential step for efficient photocatalysis [33,34]. The surface area above the curves in C/C_0 vs. time in Fig. 12 corresponds to the adsorption content of photocatalysts. As is shown in Fig. 12, TCE conversion of 0.34Ni0Ox, 0.34Ni43Ox, 0.34Ni66Ox and 0.34Ni100Ox at 40 min TOS are 0%, 88%, 42% and 77%, respectively.

Interestingly, the adsorption ability and surface area of samples with different oxide contents are in the order of 0.34Ni43Ox> 0.34Ni100Ox> 0.34Ni66Ox> 0.34Ni0Ox. The more adsorption of TCE prior to turning the light on, the higher photocatalytic activity. Adsorption and conversion of TCE on 0.34Ni43Ox is 1.7 and 2.5 times higher than 0.5Ni43Ox, respectively. From photocatalysts' adsorption capacities and surface areas, it is found that the amount of adsorbed TCE per unit of surface area for 0.34Ni0Ox and 0.34Ni43Ox

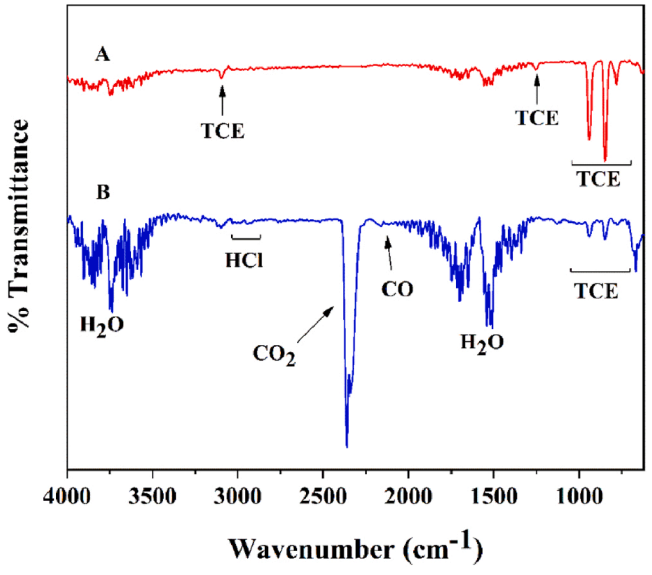

Fig. 11. FTIR spectra of 500 ppm TCE in air as feed (A) and the reactor effluent gas for 0.34Ni43Ox (B).

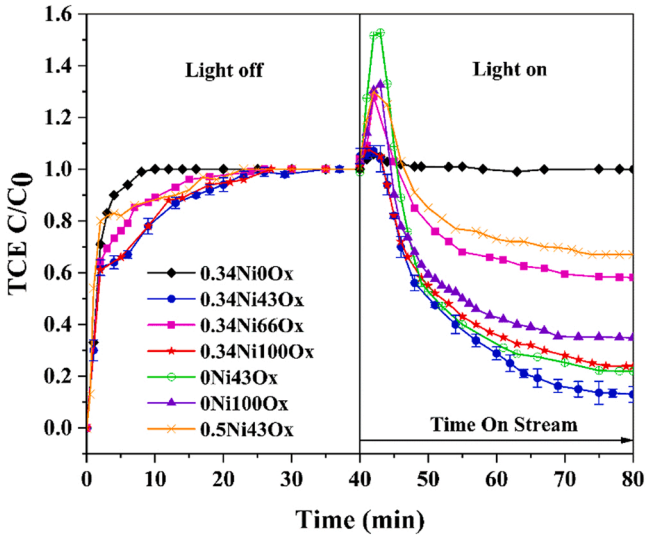

Fig. 12. Adsorption of TCE on some samples, when the light is off and photocatalytic degradation of TCE on the samples under UV light irradiation, room temperature, atmospheric pressure and GHSV of 30000 ml/h/g_{cat}.

are 1.53 and 0.59 μmole/m^2 (Table 1), which corresponds to 0.92 and 0.35 TCE molecules/nm^2, respectively. After oxidation, the number of adsorbed TCE molecules per unit of surface area was significantly reduced. The TCE has a planar molecule with 3.6 × 6.2 × 6.6 Å dimensions [108], so the number of TCE molecules that are required to cover 1 nm^2 of the surface can be between 2.4 and 4.2. An adjusted content of SnO_2 and Ni in the heterostructure is essential to improve surface characteristics as well as optical properties. The number of defects and morphology at the surface of heterostructures, resulting from oxidation and dopant content, enhance the reactant adsorption and reactions. Fig. 12 shows that when the light is switched on, the C/C_0 has a burst and then diminishes with TOS. The strong adsorption of TCE on photocatalysts acts as a reversible deactivation that mainly causes decreasing in TCE conversion with TOS [109]. Adjusting the composition of heterostructures, SnO_2 and Ni dopant contents leads to the optimized surface area, which can improve adsorption and surface reaction processes of TCE.

Several studies have been conducted to explore mechanisms of photocatalytic oxidation of TCE on TiO_2 in the air [24,31,32,43,44,45,107]. The exact mechanisms and effects of reaction intermediates and reactive species in gas-phase photocatalytic oxidation of TCE have remained unclear. The experiment runs at dark condition (Fig. 12A) show that adsorption of TCE is very fast at the initial 10 min and reaches equilibrium after an utmost of 40 min. After UV irradiation, desorption and conversion of TCE take place simultaneously due to the fast decrease in TCE amount after light irradiation (Fig. 12B). Adsorption of UV light by the heterostructures creates electrons in the conduction bands and holes in the valence bands, which can move toward the surface. It has been proposed that OH free radicals are the main responsible for initiating the degradation of TCE in humid air [43], but in air without water other reactions will be responsible for oxidation of TCE [110]. The adsorbed oxygen molecules are reduced with e^- at surface to produce oxygen radicals, which break the TCE double bond, as the initiating step of TCE oxidation in dry air. It is also established that TCE can directly react with h^+ and start photocatalytic degradation [110].

Any chlorinated reaction by-products could be detected in FTIR· H_2O is produced during the photocatalysis process and no induction period was detected in TCE degradation graphs (Fig. 12B) at the first minutes of runs after light irradiation. The induction period is a desorption dominant stage in dry air photocatalysis after light irradiation. This stage takes place to produce water for the formation of OH radicals needed for the pollutant degradation. If the OH radicals are the dominant responsible for the oxidation of pollutants, the water may not be detected in products [111].

3.3.3. *Effect of oxidation extent*

By thermal oxidation, the SnO_2 content of photocatalysts was changed to find the optimum heterostructure composition between SnS_2 and SnO_2. TCE conversions after 30 min TOS for 0.34 wt% Ni-doped samples with different oxidation percentages are exhibited in Fig. 13.

By partial oxidation up to 43%, the photocatalytic conversion increases. Oxidation enhances the surface area of 0.34Ni0Ox, which causes higher adsorption of TCE and provides more reaction-active centers on the surface. Also, a heterostructure between SnO_2 and SnS_2 can decrease the recombination rate and enhance electrons and holes separation and transfer through the interface. The heterostructure with 43% SnO_2 shows the highest photocatalytic conversion, converting TCE up to 85% after 30 min TOS. High BET surface area of 0.34Ni43Ox leads to higher adsorption of TCE and more reactive centers on the surface, which can adsorb more oxygen molecules and then provides more radical concentration. XRD, HR-TEM and Raman analysis of 0.34Ni43Ox exhibited less crystallinity and ultra-small particles. Raman spectra reveal that the particles' size and crystallinity, consequently the number of defects, depends on oxidation content. 0.34Ni43Ox heterostructure with tuned SnO_2 content, size and surface defects can quench PL emission intensity and, as a result, electron-hole pairs recombination

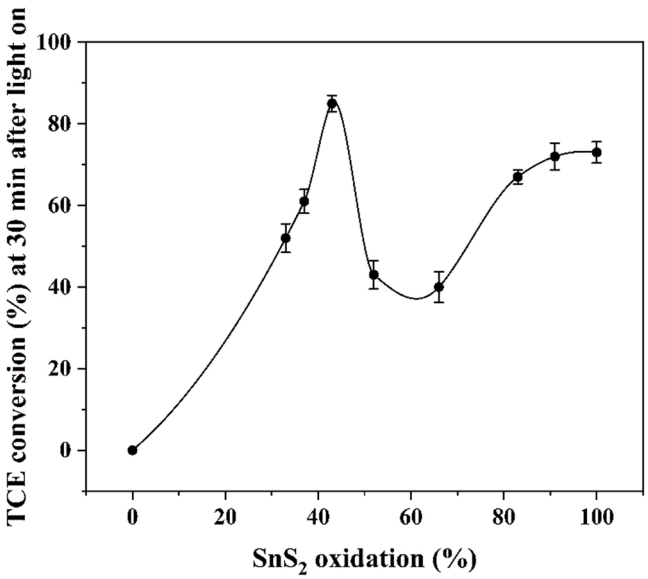

Fig. 13. TCE photocatalytic conversion after 30 min TOS for different oxide contents of 0.34NiXOx under UV light irradiation, GHSV: 30000 ml/h/g_{cat}.

probability. Tuned band gap caused by appropriate oxide content improves light-harvesting, resulting in the generation of more electrons and holes and higher conversion. By oxidation higher than the optimum amount toward pure Ni-doped SnO_2, TCE degradation decreases. For 0.34Ni66Ox, the surface area was reduced, implying larger particles. The low surface area reduces surface reactions of TCE and then photocatalytic conversion. Also, oxidation higher than 43% to 66% reduces the efficiency of electrons and holes separation, which diminishes photocatalytic degradation. When oxide content exceeds 66%, photocatalytic conversion rapidly increases and shows a plateau, 67%, 72% and 73% for 0.34Ni83Ox, 0.34Ni91Ox and 0.34Ni100Ox, respectively. As SnO_2 content passes over a determined amount, it prevents light and reactant accessibility of remaining SnS_2, so the TCE degradation behaves like the Ni-doped SnO_2 [50]. Oxidation higher than 66% increases surface area due to forming a hierarchical flower-like Ni-doped SnO_2, including many small nanoparticles, which enhance photocatalytic oxidation conversion. 0.34Ni100Ox shows 77% TCE conversion due to high surface area, providing more TCE adsorption and activation on its surface. However, PL results prove higher recombination of electron-holes pairs for 0.34Ni100Ox. Lower photogenerated charges separation efficiency does not limit photocatalytic degradation, probably due to the modified hierarchical structure that benefits from high surface area and fast charge mobility of low-path ultra-fine SnO_2 particles [9]. High surface area of oxide and more surface defects because of doping produce more reduction and oxidation centers that can overcome low carriers' recombination at bulk and surface.

3.3.4. *Effect of Ni dopant and humidity*

The effect of Ni concentration on photocatalytic degradation of TCE was investigated by increasing its content to 0.5 wt%. Fig. 14 demonstrates the TCE photocatalytic conversion of 0Ni43Ox, 0.34Ni43Ox and 0.5Ni43Ox after 30 min TOS. Contrasting 0Ni43Ox, 0.34Ni43Ox possesses higher conversion because Ni can serve as a mediator for charge transfer and trap electrons and holes to efficiently enhance the lifetime of electron-hole carriers at the bulk, interface and surface of heterostructure, as was observed in PL spectra intensities [75]. In addition, Ni dopant can reduce crystals size and increase surface area and surface defects of heterostructures to improve surface reactions and radicals concentration [8]. Ni doping can enhance light absorption, increasing the number of electrons and holes, subsequently the redox ability [66]. TCE conversion dramatically decreases for 0.5Ni43Ox. Increasing the Ni

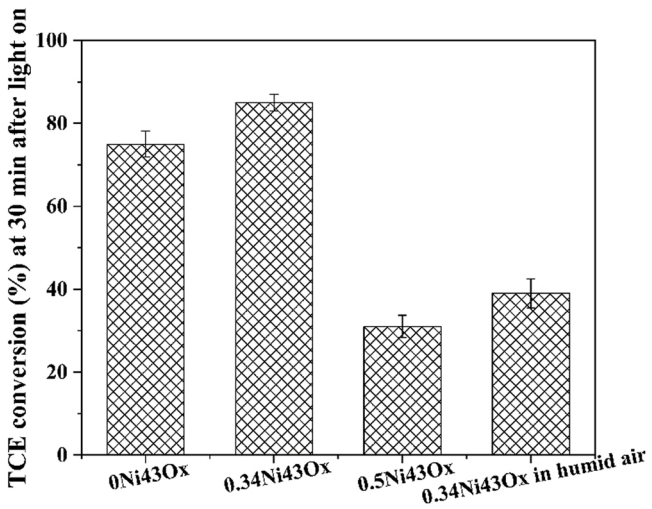

Fig. 14. Effect of the Ni content and humidity for TCE photocatalytic degradation. TCE conversion at 30 min TOS on X% Ni on 43% oxidized SnS_2, GHSV: 30000 ml/h/g_{cat}.

content reduces the distance between trapping centers, so quantum tunneling increases the recombination of electrons and holes that has also been observed in other semiconductors doping [41,75]. Furthermore, more Ni concentration can increase particles size and reduce surface area, which reduces the adsorption of oxygen molecules and TCE. It has been proved that an optimum amount of Ni dopant will decrease particles size, improve surface area, light absorption and photogenerated charges separation efficiency [66,74–76,100,112].

Zero air containing 50% RH was introduced into the reactor to investigate the water vapor effect on TCE degradation. As shown in Fig. 14, photocatalytic degradation of TCE in presence of water vapor is diminished. Water molecules can be adsorbed on the heterostructure surface by hydrogen bonding with hydroxyl groups, so water creates a multi-layer, prohibiting TCE molecules from reaching the surface and active centers [113]. Also, water molecules can compete with TCE for adsorption on active sites [114]. Another reason is that water film on the surface blocks the UV radiation, lowering light intensity [3].

3.3.5. Effect of the lamp wavelength and durability of the photocatalyst

The strength of TCE bonds, C-C, C-Cl, C-C, and C-H, are 82.6, 81.0, 145.8, 98.7 kcal $mole^{-1}$, respectively. The energy of the UV lamp, 150 kcal $mole^{-1}$, can break these bonds, while the energy of visible light is less than 72 kcal $mole^{-1}$ [115]. The effect of light wavelength on TCE degradation is shown in Fig. 15A. TCE degradation on the bare wire-mesh substrate as a blank test is negligible. Under visible light irradiation, no conversion of TCE on 0.34Ni0Ox is detected, though 0.34Ni43Ox has a considerable conversion of 18%. Tuned content heterostructure of 0.34Ni43Ox not only enhances TCE degradation under UV light but also acquires a narrow band gap to be a promising photocatalyst even under visible light irradiation.

For evaluation of 0.34Ni43Ox photocatalyst stability for TCE degradation under UV light, 4 successive runs with 40 min TOS were performed. Between two runs, the photocatalyst was exposed to zero air for 30 min, when the UV light was on. Fig. 15B presents that there is no significant decline in TCE conversion during 4 successive runs. It is found that the firm heterostructure formed between SnO_2 and SnS_2 exhibits strong structural durability and photostability. Formation of small SnO_2 particles on flower-like SnS_2 prevents the agglomeration and deactivation, improving photocatalytic conversion.

4. Conclusion

In summary, we have reported a two-step method for synthesizing Ni-doped SnO_2/SnS_2 heterostructures for the photocatalytic degradation of TCE in air. Partial oxidation was used to change the morphology, improve the surface area, and regulate surface defects for higher TCE adsorption, activation and degradation. Small particles size and less crystallinity, resulting from tuned heterostructure composition, improve defects quantity at the photocatalyst surface, leading to enhanced electron-hole separation and transition at the surface and higher reactive adsorbed oxygen. The staggered band alignment formed between SnO_2 and SnS_2 leads to retarding recombination of charge carriers at the interface. Besides, SnO_2/SnS_2 combination extended light-harvesting from UV to visible light range, which causes photoactivation of heterostructure under visible light. Adjusted content of heteroatom doping serves as trapping centers in the lattice structure, enhancing the lifetime and separation efficiency of electrons and holes, especially at the surface. Ni doping can improve the light-harvesting of SnO_2/SnS_2 heterostructures, more considerable than SnO_2 and SnS_2. Surface defects resulting from Ni doping can act as reactive centers for TCE decomposition. The sample with the tuned composition of Ni, SnS_2 and SnO_2 (0.34Ni43Ox) as a ternary photocatalyst could convert TCE up to 88% under UV and 18% under visible light irradiation.

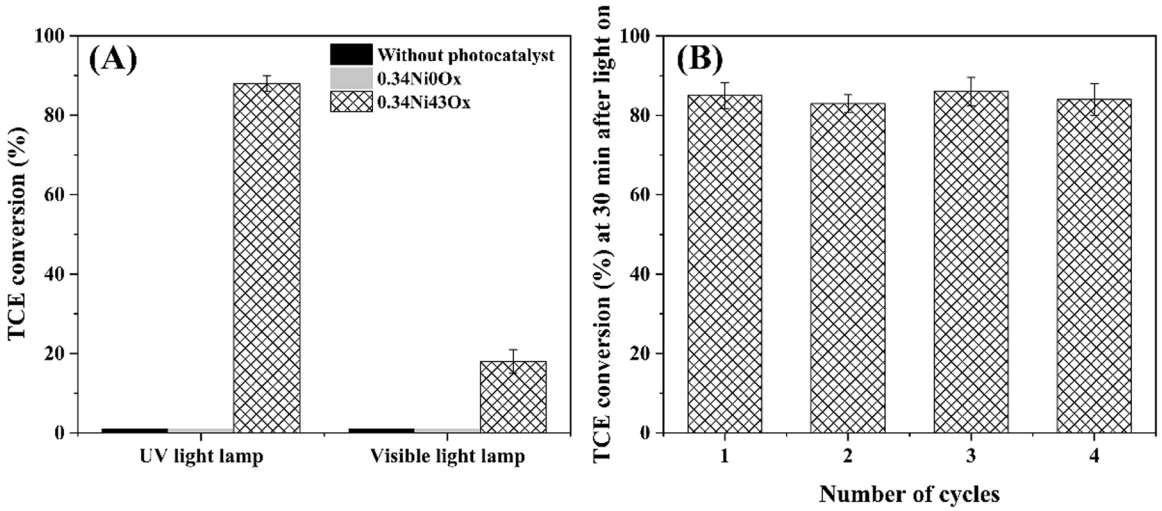

Fig. 15. Effects of lamp wavelength on TCE conversion on 0.34Ni43Ox (A) and Stability of 0.34Ni43Ox photocatalyst for the degradation of TCE under UV light irradiation (B).

CRediT authorship contribution statement

Nasim Afzali: Investigation, Methodology, Validation, Formal analysis, Visualization, Writing. **Mostafa Torka Beydokhti:** Writing – original draft, Methodology, Validation, Formal analysis, Investigation. **Abbas Ali Khodadadi:** Conceptualization, Methodology, Writing – review & editing, Supervision, Project administration, Resources. **Yadollah Mortazavi:** Methodology, Supervision, Project administration, Resources.

Declaration of Competing Interest

The authors declare that they have no known competing financial interests or personal relationships that could have appeared to influence the work reported in this paper.

Acknowledgment

A financial support from "Catalysts and Nano-structured Materials" Scientific Chair of Iranian National Science Foundation (INSF), Iran, ID 950020 is greatly appreciated.

Appendix A. Supporting information

Supplementary data associated with this article can be found in the online version at doi:10.1016/j.jece.2022.107793.

References

[1] A. Talaiekhozani, S. Rezania, K.H. Kim, R. Sanaye, A.M. Amani, Recent advances in photocatalytic removal of organic and inorganic pollutants in air, J. Clean. Prod. 278 (2021), 123895, https://doi.org/10.1016/j.jclepro.2020.123895.

[2] H. De Lasa, B. Serrano, M. Salaices, Photocatalytic Reaction Engineering, Springer, 2005, https://doi.org/10.1007/0-387-27591-6.

[3] A.H. Mamaghani, F. Haghighat, C.S. Lee, Photocatalytic oxidation technology for indoor environment air purification: the state-of-the-art, Appl. Catal. B Environ. 203 (2017) 247–269, https://doi.org/10.1016/j.apcatb.2016.10.037.

[4] J. Mo, Y. Zhang, Q. Xu, J.J. Lamson, R. Zhao, Photocatalytic purification of volatile organic compounds in indoor air: a literature review, Atmos. Environ. 43 (2009) 2229–2246, https://doi.org/10.1016/j.atmosenv.2009.01.034.

[5] IARC Working Group on the Evaluation of Carcinogenic Risks to Humans. Trichloroethylene, Tetrachloroethylene, and Some Other Chlorinated Agents, International Agency for Research on Cancer (IARC), Lyon-France, 2014. https://publications.iarc.fr/Book-And-Report-Series/Iarc-Monographs-On-The-Identification-Of-Carcinogenic-Hazards-To-Humans/Trichloroethylene-Tetrachloroethylene-And-Some-Other-Chlorinated-Agents-2014.

[6] Y. Boyjoo, H. Sun, J. Liu, V.K. Pareek, S. Wang, A review on photocatalysis for air treatment: from catalyst development to reactor design, Chem. Eng. J. 310 (2017) 537–559, https://doi.org/10.1016/j.cej.2016.06.090.

[7] S. Bai, J. Jiang, Q. Zhang, Y. Xiong, Steering charge kinetics in photocatalysis: intersection of materials syntheses, characterization techniques and theoretical simulations, Chem. Soc. Rev. 44 (2015) 2893–2939, https://doi.org/10.1039/C5CS00064E.

[8] S. Bai, N. Zhang, C. Gao, Y. Xiong, Defect engineering in photocatalytic materials, Nano Energy 53 (2018) 296–336, https://doi.org/10.1016/j.nanoen.2018.08.058.

[9] C. Sun, J. Yang, M. Xu, Y. Cui, W. Ren, J. Zhang, H. Zhao, B. Liang, Recent intensification strategies of SnO_2-based photocatalysts: a review, Chem. Eng. J. 427 (2022), 131564, https://doi.org/10.1016/j.cej.2021.131564.

[10] H. Wang, L. Zhang, Z. Chen, J. Hu, S. Li, Z. Wang, J. Liu, X. Wang, Semiconductor heterojunction photocatalysts: design, construction, and photocatalytic performances, Chem. Soc. Rev. 43 (2014) 5234–5244, https://doi.org/10.1039/C4CS00126E.

[11] Y. Qu, X. Duan, Progress, challenge and perspective of heterogeneous photocatalysts, Chem. Soc. Rev. 42 (2013) 2568–2580, https://doi.org/10.1039/c2cs35355e.

[12] M. Farooq, I.A. Raja, A. Pervez, Photocatalytic degradation of TCE in water using TiO_2 catalyst, Sol. Energy 83 (2009) 1527–1533, https://doi.org/10.1016/j.solener.2009.04.009.

[13] Y.-C. Hsu, S.-H. Chang, W.-C. Chung, M.-B. Chang, Photocatalytic removal of trichloroethylene from water with $LaFeO_3$, Environ. Sci. Pollut. Res. 26 (2019) 26276–26285, https://doi.org/10.1007/S11356-019-05886-5.

[14] W. Jiang, P. Tang, S. Lyu, M.L. Brusseau, Y. Xue, X. Zhang, Z. Qiu, Q. Sui, Enhanced redox degradation of chlorinated hydrocarbons by the Fe(II)-catalyzed calcium peroxide system in the presence of formic acid and citric acid, J. Hazard. Mater. 368 (2019) 506–513, https://doi.org/10.1016/j.jhazmat.2019.01.057.

[15] M. Raciulete, F. Papa, D. Kawamoto, C. Munteanu, D.C. Culita, C. Negrila, I. Atkinson, V. Bratan, J. Pandele-Cusu, I. Balint, Particularities of trichloroethylene photocatalytic degradation over crystalline $RbLaTa_2O_7$ nanowire bundles grown by solid-state synthesis route, J. Environ. Chem. Eng. 7 (2019), 102789, https://doi.org/10.1016/J.JECE.2018.11.034.

[16] J. Niu, L. Yin, Y. Dai, Y. Bao, J.C. Crittenden, Design of visible light responsive photocatalysts for selective reduction of chlorinated organic compounds in water, Appl. Catal. A Gen. 521 (2016) 90–95, https://doi.org/10.1016/J.APCATA.2015.11.018.

[17] B. Jung, W. Deng, Y. Li, B. Batchelor, A. Abdel-Wahab, Simulated solar light-driven photocatalytic degradation of trichloroethylene in water using BiOBr promoted by sulfite addition, Environ. Sci. Eur. 32 (2020) 1–15, https://doi.org/10.1186/S12302-019-0287-9.

[18] R. State, F. Papa, T. Tabakova, I. Atkinson, C. Negrila, I. Balint, Photocatalytic abatement of trichlorethylene over Au and Pd–Au supported on TiO_2 by combined photomineralization/hydrodechlorination reactions under simulated solar irradiation, J. Catal. 346 (2017) 101–108, https://doi.org/10.1016/J.JCAT.2016.11.032.

[19] Y. Zhang, S.J. Park, Au–pd bimetallic alloy nanoparticle-decorated $BiPO_4$ nanorods for enhanced photocatalytic oxidation of trichloroethylene, J. Catal. 355 (2017) 1–10, https://doi.org/10.1016/J.JCAT.2017.08.007.

[20] Y. Zhang, S.J. Park, Bimetallic AuPd alloy nanoparticles deposited on MoO_3 nanowires for enhanced visible-light driven trichloroethylene degradation, J. Catal. 361 (2018) 238–247, https://doi.org/10.1016/J.JCAT.2018.03.010.

[21] V. Héquet, C. Raillard, O. Debono, F. Thévenet, N. Locoge, L. Le Coq, Photocatalytic oxidation of VOCs at ppb level using a closed-loop reactor: the mixture effect, Appl. Catal. B Environ. 226 (2018) 473–486, https://doi.org/10.1016/J.APCATB.2017.12.041.

[22] S. Suárez, N. Arconada, Y. Castro, J.M. Coronado, R. Portela, A. Durán, B. Sánchez, Photocatalytic degradation of TCE in dry and wet air conditions with TiO_2 porous thin films, Appl. Catal. B Environ. 108–109 (2011) 14–21, https://doi.org/10.1016/j.apcatb.2011.07.027.

[23] O. Debono, V. Hequet, L. Le Coq, N. Locoge, F. Thevenet, VOC ternary mixture effect on ppb level photocatalytic oxidation: removal kinetic, reaction intermediates and mineralization, Appl. Catal. B Environ. 218 (2017) 359–369, https://doi.org/10.1016/j.apcatb.2017.06.070.

[24] H.H. Ou, S.L. Lo, Photocatalysis of gaseous trichloroethylene (TCE) over TiO_2: The effect of oxygen and relative humidity on the generation of dichloroacetyl chloride (DCAC) and phosgene, J. Hazard. Mater. 146 (2007) 302–308, https://doi.org/10.1016/j.jhazmat.2006.12.039.

[25] K. Demeestere, A. De Visscher, J. Dewulf, M. Van Leeuwen, H. Van Langenhove, A new kinetic model for titanium dioxide mediated heterogeneous photocatalytic degradation of trichloroethylene in gas-phase, Appl. Catal. B Environ. 54 (2004) 261–274, https://doi.org/10.1016/j.apcatb.2004.06.020.

[26] S.B. Kim, S.C. Hong, Kinetic study for photocatalytic degradation of volatile organic compounds in air using thin film TiO_2 photocatalyst, Appl. Catal. B Environ. 35 (2002) 305–315, https://doi.org/10.1016/S0926-3373(01)00274-0.

[27] L.A. Dibble1, G.B. Raupp, Fluidized-bed photocatalytic oxidation of trichloroethylene in contaminated air streams, Environ. Sci. Technol. 26 (1992) 492–495, https://doi.org/10.1021/es00027a006.

[28] M.D. Hernández-Alonso, S. García-Rodríguez, S. Suárez, R. Portela, B. Sánchez, J. M. Coronado, Highly selective one-dimensional TiO_2-based nanostructures for air treatment applications, Appl. Catal. B Environ. 110 (2011) 251–259, https://doi.org/10.1016/j.apcatb.2011.09.009.

[29] V. Puddu, H. Choi, D.D. Dionysiou, G.L. Puma, TiO_2 photocatalyst for indoor air remediation: Influence of crystallinity, crystal phase, and UV radiation intensity on trichloroethylene degradation, Appl. Catal. B Environ. 94 (2010) 211–218, https://doi.org/10.1016/J.APCATB.2009.08.003.

[30] A.J. Maira, K.L. Yeung, C.Y. Lee, P.L. Yue, C.K. Chan, Size effects in gas-phase photo-oxidation of trichloroethylene using nanometer-sized TiO_2 catalysts, J. Catal. 192 (2000) 185–196, https://doi.org/10.1006/JCAT.2000.2838.

[31] S. Suárez, J.M. Coronado, R. Portela, J.C. Martín, M. Yates, P. Avila, B. Sánchez, On the preparation of TiO_2−sepiolite hybrid materials for the photocatalytic degradation of TCE: influence of TiO_2 distribution in the mineralization, Environ. Sci. Technol. 42 (2008) 5892–5896, https://doi.org/10.1021/ES703257W.

[32] M. Mohseni, Gas phase trichloroethylene (TCE) photooxidation and byproduct formation: Photolysis vs. titania/silica based photocatalysis, Chemosphere 59 (2005) 335–342, https://doi.org/10.1016/j.chemosphere.2004.10.054.

[33] I. Jansson, S. Suárez, F.J. Garcia-Garcia, B. Sánchez, Zeolite-TiO_2 hybrid composites for pollutant degradation in gas phase, Appl. Catal. B Environ. 178 (2015) 100–107, https://doi.org/10.1016/j.apcatb.2014.10.022.

[34] I. Jansson, K. Kobayashi, H. Hori, B. Sánchez, B. Ohtani, S. Suárez, Decahedral anatase titania particles immobilized on zeolitic materials for photocatalytic degradation of VOC, Catal. Today 287 (2017) 22–29, https://doi.org/10.1016/j.cattod.2016.11.041.

[35] V. Puddu, R. Mokaya, G. Li Puma, Novel one step hydrothermal synthesis of TiO_2/WO_3 nanocomposites with enhanced photocatalytic activity, Chem. Commun. (2007) 4749–4751, https://doi.org/10.1039/b711559h.

[36] I. Jansson, K. Yoshiiri, H. Hori, F.J. García-García, S. Rojas, B. Sánchez, B. Ohtani, S. Suárez, Visible light responsive Zeolite/WO_3-Pt hybrid photocatalysts for degradation of pollutants in air, Appl. Catal. A Gen. 521 (2016) 208–219, https://doi.org/10.1016/j.apcata.2015.12.015.

[37] H.H. Ou, S.L. Lo, Effect of Pt/Pd-doped TiO_2 on the photocatalytic degradation of trichloroethylene, J. Mol. Catal. A Chem. 275 (2007) 200–205, https://doi.org/10.1016/J.MOLCATA.2007.05.044.

[38] T. Seyama, T. Tanimura, K. Tashiro, S. Yamazaki, Photocatalytic degradation of trichloroethylene on platinum ion-doped TiO_2 under visible light irradiation, Res. Chem. Intermed. 43 (2017) 5025–5039, https://doi.org/10.1007/S11164-017-3051-Z.

[39] H. Sun, R. Ullah, S. Chong, H.M. Ang, M.O. Tadé, S. Wang, Room-light-induced indoor air purification using an efficient Pt/N-TiO_2 photocatalyst, Appl. Catal. B Environ. 108–109 (2011) 127–133, https://doi.org/10.1016/j.apcatb.2011.08.017.

[40] T. Tanimura, A. Yoshida, S. Yamazaki, Reduced formation of undesirable by-products from photocatalytic degradation of trichloroethylene, Appl. Catal. B Environ. 61 (2005) 346–351, https://doi.org/10.1016/J.APCATB.2005.05.015.

[41] A. Banisharif, A.A. Khodadadi, Y. Mortazavi, A. Anaraki Firooz, J. Beheshtian, S. Agah, S. Menbari, Highly active Fe_2O_3-doped TiO_2 photocatalyst for degradation of trichloroethylene in air under UV and visible light irradiation: experimental and computational studies, Appl. Catal. B Environ. 165 (2015) 209–221, https://doi.org/10.1016/j.apcatb.2014.10.023.

[42] S.E. Park, H. Joo, J.W. Kang, Effect of impurities in TiO_2 thin films on trichloroethylene conversion, Sol. Energy Mater. Sol. Cells 83 (2004) 39–53, https://doi.org/10.1016/J.SOLMAT.2004.02.012.

[43] K. Tashiro, T. Tanimura, S. Yamazaki, Photocatalytic degradation of gaseous trichloroethylene on porous titanium dioxide pellets modified with copper(II) under visible light irradiation, J. Photochem. Photobiol. A Chem. 377 (2019) 228–235, https://doi.org/10.1016/j.jphotochem.2019.03.037.

[44] T.H. Lim, S.D. Kim, Trichloroethylene degradation by photocatalysis in annular flow and annulus fluidized bed photoreactors, Chemosphere 54 (2004) 305–312, https://doi.org/10.1016/S0045-6535(03)00753-7.

[45] W.S. Yoon, H.S. Lee, K. Choi, T.K. Lee, In-situ observation of photocatalysis of gaseous trichloroethylene using a fourier transform infrared in the presence of a visible light responding homemade oxynitride doped TiO_2 under blue LED and violet LED irradiations, J. Mater. Res. Technol. 10 (2021) 15–23, https://doi.org/10.1016/j.jmrt.2020.11.094.

[46] Y. Wang, Q. Wang, X. Zhan, F. Wang, M. Safdar, J. He, Visible light driven type II heterostructures and their enhanced photocatalysis properties: a review, Nanoscale 5 (2013) 8326–8339, https://doi.org/10.1039/C3NR01577G.

[47] Y.C. Zhang, Z.N. Du, M. Zhang, Hydrothermal synthesis of SnO_2/SnS_2 nanocomposite with high visible light-driven photocatalytic activity, Mater. Lett. 65 (2011) 2891–2894, https://doi.org/10.1016/J.MATLET.2011.06.049.

[48] Y.C. Zhang, L. Yao, G. Zhang, D.D. Dionysiou, J. Li, X. Du, One-step hydrothermal synthesis of high-performance visible-light-driven SnS_2/SnO_2 nanoheterojunction photocatalyst for the reduction of aqueous Cr(VI), Appl. Catal. B Environ. 144 (2014) 730–738, https://doi.org/10.1016/j.apcatb.2013.08.006.

[49] G. Zhang, D. Chen, N. Li, Q. Xu, H. Li, J. He, J. Lu, SnS_2/SnO_2 heterostructured nanosheet arrays grown on carbon cloth for efficient photocatalytic reduction of Cr(VI), J. Colloid Interface Sci. 514 (2018) 306–315, https://doi.org/10.1016/j.jcis.2017.12.045.

[50] Y.C. Zhang, Z.N. Du, K.W. Li, M. Zhang, D.D. Dionysiou, High-performance visible-light-driven SnS_2/SnO_2 nanocomposite photocatalyst prepared via in situ hydrothermal oxidation of SnS_2 nanoparticles, ACS Appl. Mater. Interfaces 3 (2011) 1528–1537, https://doi.org/10.1021/am200102y.

[51] R.K. Chava, J.Y. Do, M. Kang, Enhanced photoexcited carrier separation in CdS–SnS_2 heteronanostructures: a new 1D–0D visible-light photocatalytic system for the hydrogen evolution reaction, J. Mater. Chem. A 7 (2019) 13614–13628, https://doi.org/10.1039/C9TA03059J.

[52] K. Hu, C. Ming, Y. Liu, C. Zheng, S. Zhang, D. Wang, W. Zhao, F. Huang, Introducing sulfur vacancies and in-plane SnS_2/SnO_2 heterojunction in SnS_2 nanosheets to promote photocatalytic activity, Chin. Chem. Lett. 31 (2020) 2809–2813, https://doi.org/10.1016/J.CCLET.2020.07.052.

[53] N. Bao, L. Shen, T. Takata, K. Domen, Self-templated synthesis of nanoporous CdS nanostructures for highly efficient photocatalytic hydrogen production under visible light, Chem. Mater. 20 (2008) 110–117, https://doi.org/10.1021/cm7029344.

[54] Y. Liu, D. Pan, M. Xiong, Y. Tao, X. Chen, D. Zhang, Y. Huang, G. Li, In-situ fabrication SnO_2/SnS_2 heterostructure for boosting the photocatalytic degradation of pollutants, Chin. J. Catal. 41 (2020) 1554–1563, https://doi.org/10.1016/S1872-2067(19)63498-4.

[55] S. Wang, G. Li, Z. Leng, Y. Wang, S. Fang, J. Wang, Y. Wei, L. Li, Systematic optimization of promoters in trace SnS_2 coating SnO_2 nano-heterostructure for high performance Cr(VI) photoreduction, Appl. Surf. Sci. 471 (2019) 813–821, https://doi.org/10.1016/j.apsusc.2018.12.042.

[56] R. Huang, C. Wu, S. Huang, D. Chen, Q. Zhang, Q. Wang, Z. Hu, Y. Jiang, B. Zhao, Z. Chen, IUCr, Construction of SnS_2–SnO_2 heterojunctions decorated on graphene nanosheets with enhanced visible-light photocatalytic performance, Acta Cryst. 75 (2019) 812–821, https://doi.org/10.1107/S2053229619006399.

[57] L. Yang, J. Huang, L. Shi, L. Cao, W. Zhou, K. Chang, X. Meng, G. Liu, Y. Jie, J. Ye, Efficient hydrogen evolution over Sb doped SnO_2 photocatalyst sensitized by Eosin Y under visible light irradiation, Nano Energy 36 (2017) 331–340, https://doi.org/10.1016/j.nanoen.2017.04.039.

[58] X. Zhang, P. Zhang, L. Wang, H. Gao, J. Zhao, C. Liang, J. Hu, G. Shao, Template- oriented synthesis of monodispersed SnS_2@SnO_2 hetero-nanoflowers for Cr(VI) photoreduction, Appl. Catal. B Environ. 192 (2016) 17–25, https://doi.org/ 10.1016/j.apcatb.2016.03.035.

[59] Y.Y. Li, J.G. Wang, H.H. Sun, W. Hua, X.R. Liu, Heterostructured SnS_2/SnO_2 nanotubes with enhanced charge separation and excellent photocatalytic hydrogen production, Int. J. Hydrog. Energy 43 (2018) 14121–14129, https://doi.org/10.1016/j.ijhydene.2018.05.130.

[60] L. Mao, J. Li, Y. Xie, Y. Zhong, Y. Hu, Controllable growth of SnS_2/SnO_2 heterostructured nanoplates via a hydrothermal-assisted self-hydrolysis process and their visible-light-driven photocatalytic reduction of Cr(vi), RSC Adv. 4 (2014) 29698–29701, https://doi.org/10.1039/c4ra03943b.

[61] L. Yao, Y.C. Zhang, J. Li, Y. Chen, Photocatalytic properties of SnS_2/SnO_2 nanocomposite prepared by thermal oxidation of SnS_2 nanoparticles in air, Sep. Purif. Technol. 122 (2014) 1–5, https://doi.org/10.1016/j.seppur.2013.10.038.

[62] J. Mu, F. Teng, H. Miao, Y. Wang, X. Hu, In-situ oxidation fabrication of 0D/2D SnO_2/SnS_2 novel Step-scheme heterojunctions with enhanced photoelectrochemical activity for water splitting, Appl. Surf. Sci. 501 (2020), 143974, https://doi.org/10.1016/j.apsusc.2019.143974.

[63] N. Ojha, A. Bajpai, S. Kumar, Enriched oxygen vacancies of Cu_2O/SnS_2/SnO_2 heterostructure for enhanced photocatalytic reduction of CO_2 by water and nitrogen fixation, J. Colloid Interface Sci. 585 (2021) 764–777, https://doi.org/10.1016/j.jcis.2020.10.056.

[64] Y. Wang, Y. Su, W. Fang, Y. Zhang, X. Li, G. Zhang, W. Sun, SnO_2/SnS_2 nanocomposite anchored on nitrogen-doped RGO for improved photocatalytic reduction of aqueous Cr(VI), Powder Technol. 363 (2020) 337–348, https://doi.org/10.1016/j.powtec.2020.01.009.

[65] D. Chen, S. Huang, R. Huang, Q. Zhang, T.T. Le, E. Cheng, R. Yue, Z. Hu, Z. Chen, Construction of Ni-doped SnO_2-SnS_2 heterojunctions with synergistic effect for enhanced photodegradation activity, J. Hazard. Mater. 368 (2019) 204–213, https://doi.org/10.1016/j.jhazmat.2019.01.009.

[66] D. Chen, S. Huang, R. Huang, Q. Zhang, T.T. Le, E. Cheng, Z. Hu, Z. Chen, Convenient fabrication of Ni-doped SnO_2 quantum dots with improved photodegradation performance for Rhodamine B, J. Alloy. Compd. 788 (2019) 929–935, https://doi.org/10.1016/j.jallcom.2019.02.193.

[67] S. Bai, Y. Xiong, Recent advances in two-dimensional nanostructures for catalysis applications, Sci. Adv. Mater. 7 (2015) 2168–2181, https://doi.org/10.1166/SAM.2015.2261.

[68] J. Shi, X. Wang, S. Zhang, L. Xiao, Y. Huan, Y. Gong, Z. Zhang, Y. Li, X. Zhou, M. Hong, Q. Fang, Q. Zhang, X. Liu, L. Gu, Z. Liu, Y. Zhang, Two-dimensional metallic tantalum disulfide as a hydrogen evolution catalyst, Nat. Commun. 8 (2017), https://doi.org/10.1038/s41467-017-01089-z.

[69] H. Bin Wu, J.S. Chen, X.W. (David) Lou, H.H. Hng, Synthesis of SnO_2 hierarchical structures assembled from nanosheets and their lithium storage properties, J. Phys. Chem. C 115 (2011) 24605–24610, https://doi.org/10.1021/JP208158M.

[70] E. Abdelkader, L. Nadjia, B. Naceur, B. Noureddine, SnO_2 foam grain-shaped nanoparticles: Synthesis, characterization and UVA light induced photocatalysis, J. Alloy. Compd. 679 (2016) 408–419, https://doi.org/10.1016/j.jallcom.2016.04.016.

[71] S.P. Kim, M.Y. Choi, H.C. Choi, Photocatalytic activity of SnO_2 nanoparticles in methylene blue degradation, Mater. Res. Bull. 74 (2016) 85–89, https://doi.org/10.1016/j.materresbull.2015.10.024.

[72] X. Li, N. Kikugawa, J. Ye, A comparison study of rhodamineB photodegradation over nitrogen-doped lamellar niobic acid and titanic acid under visible-light irradiation, Chem. A Eur. J. 15 (2009) 3538–3545, https://doi.org/10.1002/CHEM.200801770.

[73] A. Zhang, R. He, H. Li, Y. Chen, T. Kong, K. Li, H. Ju, J. Zhu, W. Zhu, J. Zeng, Nickel doping in atomically thin tin disulfide nanosheets enables highly efficient CO_2 reduction, Angew. Chem. 130 (2018) 11120–11124, https://doi.org/10.1002/ANGE.201806043.

[74] M. Kandasamy, A. Seetharaman, D. Sivasubramanian, A. Nithya, K. Jothivenkatachalam, N. Maheswari, M. Gopalan, S. Dillibabu, A. Eftekhari, Ni-doped SnO_2 nanoparticles for sensing and photocatalysis, ACS Appl. Nano Mater. 1 (2018) 5823–5836, https://doi.org/10.1021/acsanm.8b01473.

[75] H. Chen, L. Ding, W. Sun, Q. Jiang, J. Hu, J. Li, Synthesis and characterization of Ni doped SnO_2 microspheres with enhanced visible-light photocatalytic activity, RSC Adv. 5 (2015) 56401–56409, https://doi.org/10.1039/c5ra10268e.

[76] L. Meng, S. Wang, F. Cao, W. Tian, R. Long, L. Li, Doping-induced amorphization, vacancy, and gradient energy band in SnS_2 nanosheet arrays for improved photoelectrochemical water splitting, Angew. Chem. Int. Ed. 58 (2019) 6761–6765, https://doi.org/10.1002/anie.201902411.

[77] M. Setayeshmehr, M. Haghighi, K. Mirabbaszadeh, Binder-free 3D flower-like alkali doped- SnS_2 electrodes for high-performance supercapacitors, Electrochim. Acta 376 (2021), https://doi.org/10.1016/j.electacta.2021.137987.

[78] Y. Liu, Y. Zhou, X. Zhou, X. Jin, B. Li, J. Liu, G. Chen, Cu doped SnS_2 nanostructure induced sulfur vacancy towards boosted photocatalytic hydrogen evolution, Chem. Eng. J. 407 (2021), https://doi.org/10.1016/j.cej.2020.127180.

[79] L. Ma, L. Xu, X. Zhou, X. Xu, L. Zhang, Molybdenum-doped few-layered SnS_2 architectures with enhanced electrochemical supercapacitive performance, RSC Adv. 5 (2015) 105862–105868, https://doi.org/10.1039/c5ra18634j.

[80] I. Shown, S. Samireddi, Y.C. Chang, R. Putikam, P.H. Chang, A. Sabbah, F.Y. Fu, W.F. Chen, C.I. Wu, T.Y. Yu, P.W. Chung, M.C. Lin, L.C. Chen, K.H. Chen, Carbon-doped SnS_2 nanostructure as a high-efficiency solar fuel catalyst under visible light, Nat. Commun. 9 (2018), https://doi.org/10.1038/s41467-017-02547-4.

[81] J. Zai, X. Qian, K. Wang, C. Yu, L. Tao, Y. Xiao, J. Chen, 3D-hierarchical SnS_2 micro/nano-structures: controlled synthesis, formation mechanism and lithium ion storage performances, CrystEngComm 14 (2012) 1364–1375, https://doi.org/10.1039/c1ce05950e.

[82] W. Zhu, Y. Yang, D. Ma, H. Wang, Y. Zhang, H. Hu, Controlled growth of flower-like SnS_2 hierarchical structures with superior performance for lithium-ion battery applications, Ionics 21 (2015) 19–26, https://doi.org/10.1007/s11581-014-1163-7.

[83] L. Yongqian, S. Shuyan, F. Weiqiang, X. Yan, Z. Hongjie, Facile synthesis and assemblies of flowerlike SnS_2 and In^{3+}-Doped SnS_2: hierarchical structures and their enhanced photocatalytic property, J. Phys. Chem. C 113 (2009) 1280–1285, https://doi.org/10.1021/jp8079974.

[84] D. Guan, J. Li, X. Gao, Y. Xie, C. Yuan, Growth characteristics and influencing factors of 3D hierarchical flower-like SnS_2 nanostructures and their superior lithium-ion intercalation performance, J. Alloy. Compd. 658 (2016) 190–197, https://doi.org/10.1016/j.jallcom.2015.10.222.

[85] J. Mu, H. Miao, E. Liu, J. Feng, F. Teng, D. Zhang, Y. Kou, Y. Jin, J. Fan, X. Hu, Enhanced light trapping and high charge transmission capacities of novel structures for efficient photoelectrochemical water splitting, Nanoscale 10 (2018) 11881–11893, https://doi.org/10.1039/c8nr03040e.

[86] Y.B. Yang, J.K. Dash, A.J. Littlejohn, Y. Xiang, Y. Wang, J. Shi, L.H. Zhang, K. Kisslinger, T.M. Lu, G.C. Wang, Large single crystal SnS_2 flakes synthesized from coevaporation of Sn and S, Cryst. Growth Des. 16 (2016) 961–973, https://doi.org/10.1021/acs.cgd.5b01512.

[87] K. Vijayarangamuthu, S. Rath, Nanoparticle size, oxidation state, and sensing response of tin oxide nanopowders using Raman spectroscopy, J. Alloy. Compd. 610 (2014) 706–712, https://doi.org/10.1016/j.jallcom.2014.04.187.

[88] L. Abello, B. Bochu, A. Gaskov, S. Koudryavtseva, G. Lucazeau, M. Roumyantseva, Structural characterization of nanocrystalline SnO_2 by X-ray and Raman spectroscopy, J. Solid State Chem. 135 (1998) 78–85, https://doi.org/10.1006/jssc.1997.7596.

[89] V. Bonu, A. Das, A.K. Sivadasan, A.K. Tyagi, S. Dhara, Invoking forbidden modes in SnO_2 nanoparticles using tip enhanced Raman spectroscopy, J. Raman Spectrosc. 46 (2015) 1037–1040, https://doi.org/10.1002/jrs.4747.

[90] A. Diéguez, A. Romano-Rodríguez, A. Vilà, J.R. Morante, The complete Raman spectrum of nanometric SnO_2 particles, J. Appl. Phys. 90 (2001) 1550–1557, https://doi.org/10.1063/1.1385573.

[91] K. Yu, Y. Xiong, Microstructural change of nano grain assemblages with the annealing temperature, Phys. Rev. B Condens. Matter Mater. Phys. 55 (1997) 2666–2671, https://doi.org/10.1103/PhysRevB.55.2666.

[92] J.X. Wang, D.F. Liu, X.Q. Yan, H.J. Yuan, L.J. Ci, Z.P. Zhou, Y. Gao, L. Song, L. F. Liu, W.Y. Zhou, G. Wang, S.S. Xie, Growth of SnO_2 nanowires with uniform branched structures, Solid State Commun. 130 (2004) 89–94, https://doi.org/10.1016/j.ssc.2004.01.003.

[93] H. Mousavi, Y. Mortazavi, A.A. Khodadadi, M.H. Saberi, S. Alirezaei, Enormous enhancement of Pt/SnO_2 sensors response and selectivity by their reduction, to CO in automotive exhaust gas pollutants including CO, NO_x and C_3H_8, Appl. Surf. Sci. 546 (2021), 149120, https://doi.org/10.1016/j.apsusc.2021.149120.

[94] R.N. Mariammal, K. Ramachandran, B. Renganathan, D. Sastikumar, On the enhancement of ethanol sensing by CuO modified SnO_2 nanoparticles using fiber-optic sensor, Sens. Actuators B Chem. 169 (2012) 199–207, https://doi.org/10.1016/j.snb.2012.04.067.

[95] L.Z. Liu, X.L. Wu, F. Gao, J.C. Shen, T.H. Li, P.K. Chu, Determination of surface oxygen vacancy position in SnO_2 nanocrystals by Raman spectroscopy, Solid State Commun. 151 (2011) 811–814, https://doi.org/10.1016/j.ssc.2011.03.029.

[96] Y. Yang, X.A. Yang, D. Leng, S.B. Wang, W.B. Zhang, Fabrication of $g\text{-}C_3N_4/SnS_2/SnO_2$ nanocomposites for promoting photocatalytic reduction of aqueous Cr(VI) under visible light, Chem. Eng. J. 335 (2018) 491–500, https://doi.org/10.1016/j.cej.2017.10.173.

[97] S. Wang, B. Yang, Y. Liu, Synthesis of a hierarchical SnS_2 nanostructure for efficient adsorption of Rhodamine B dye, J. Colloid Interface Sci. 507 (2017) 225–233, https://doi.org/10.1016/j.jcis.2017.07.053.

[98] L. Lu, X. Xu, J. Yan, F.N. Shi, Y. Huo, Oxygen vacancy rich Cu_2O based composite material with nitrogen doped carbon as matrix for photocatalytic H_2 production and organic pollutant removal, Dalton Trans. 47 (2018) 2031–2038, https://doi.org/10.1039/c7dt03835f.

[99] M. Chen, X. Wang, Y.H. Yu, Z.L. Pei, X.D. Bai, C. Sun, R.F. Huang, L.S. Wen, X-ray photoelectron spectroscopy and auger electron spectroscopy studies of Al-doped

[100] K. Srinivas, S.M. Rao, P.V. Reddy, Structural, electronic and magnetic properties of $Sn_{0.95}Ni_{0.05}O_2$ nanorods, Nanoscale 3 (2011) 642–653, https://doi.org/10.1039/c0nr00597e.

[101] G. Mohan Kumar, F. Xiao, P. Ilanchezhiyan, S. Yuldashev, A. Madhan Kumar, H. D. Cho, D.J. Lee, T.W. Kang, High performance photodiodes based on chemically processed Cu doped SnS_2 nanoflakes, Appl. Surf. Sci. 455 (2018) 446–454, https://doi.org/10.1016/j.apsusc.2018.05.197.

[102] A.A. Ziabari, F.E. Ghodsi, Synthesis and characterization of nanocrystalline CdZnO thin films prepared by sol-gel dip-coating process, in: Thin Solid Films, Elsevier, 2011, pp. 1228–1232, https://doi.org/10.1016/j.tsf.2011.06.075.

[103] A. Sadeghzadeh-Attar, M.R. Bafandeh, The effect of annealing temperature on the structure and optical properties of well-aligned 1D SnO_2 nanowires synthesized using template-assisted deposition, CrystEngComm 20 (2018) 460–469, https://doi.org/10.1039/C7CE01815K.

[104] M. Periyasamy, A. Kar, Modulating the properties of SnO_2 nanocrystals: morphological effects on structural, photoluminescence, photocatalytic, electrochemical and gas sensing properties, J. Mater. Chem. C 8 (2020) 4604–4635, https://doi.org/10.1039/C9TC06469A.

[105] A.G. Habte, F.G. Hone, F.B. Dejene, Influence of annealing temperature on the structural, morphological and optical properties of SnO_2 nanoparticles, Phys. B Condens. Matter 580 (2020), 411760, https://doi.org/10.1016/j.physb.2019.411760.

[106] N.S. Gultom, H. Abdullah, D.H. Kuo, Enhanced photocatalytic hydrogen production of noble-metal free Ni-doped Zn(O,S) in ethanol solution, Int. J. Hydrog. Energy 42 (2017) 25891–25902, https://doi.org/10.1016/j.ijhydene.2017.08.198.

[107] J. Fan, J.T. Yates, Mechanism of photooxidation of trichloroethylene on TiO_2: detection of intermediates by infrared spectroscopy, J. Am. Chem. Soc. 118 (1996) 4686–4692, https://doi.org/10.1021/ja952155q.

[108] T. Karanfil, S.A. Dastgheib, D. Mauldin, Exploring molecular sieve capabilities of activated carbon fibers to reduce the impact of NOM preloading on trichloroethylene adsorption, Environ. Sci. Technol. 40 (2006) 1321–1327, https://doi.org/10.1021/ES051285O/SUPPL_FILE/ES051285OSI20051025_113638.PDF.

[109] E. Piera, J. Ayllón, X. Doménech, J. Peral, TiO_2 deactivation during gas-phase photocatalytic oxidation of ethanol, Catal. Today 76 (2002) 259–270, https://doi.org/10.1016/S0920-5861(02)00224-9.

[110] H. Liu, S. Cheng, J. Zhang, C. Cao, W. Jiang, The gas-photocatalytic degradation of trichloroethylene without water, Chemosphere 35 (1997) 2881–2889, https://doi.org/10.1016/S0045-6535(97)00364-0.

[111] A. Enesca, Y. Yamaguchi, C. Terashima, A. Fujishima, K. Nakata, A. Duta, Enhanced UV–Vis photocatalytic performance of the $CuInS_2/TiO_2/SnO_2$ heterostructure for air decontamination, J. Catal. 350 (2017) 174–181, https://doi.org/10.1016/J.JCAT.2017.02.015.

[112] D. Khan, A. Rehman, M.Z. Rafiq, A.M. Khan, M. Ali, Improving the optical properties of SnO_2 nanoparticles through Ni doping by sol-gel technique, Curr. Res. Green. Sustain. Chem. 4 (2021), 100079, https://doi.org/10.1016/j.crgsc.2021.100079.

[113] T.N. Obee, S.O. Hay, Effects of moisture and temperature on the photooxidation of ethylene on titania, Environ. Sci. Technol. 31 (1997) 2034–2038, https://doi.org/10.1021/es960827m.

[114] N. Quici, M.L. Vera, H. Choi, G.L. Puma, D.D. Dionysiou, M.I. Litter, H. Destaillats, Effect of key parameters on the photocatalytic oxidation of toluene at low concentrations in air under 254 + 185 nm UV irradiation, Appl. Catal. B Environ. 95 (2010) 312–319, https://doi.org/10.1016/j.apcatb.2010.01.009.

[115] Y. Ku, C.M. Ma, Y.S. Shen, Decomposition of gaseous trichloroethylene in a photoreactor with TiO_2-coated nonwoven fiber textile, Appl. Catal. B Environ. 34 (2001) 181–190, https://doi.org/10.1016/S0926-3373(01)00216-8.